

Copyright
by
Sonia Quadery
2007

**The Dissertation Committee for Sonia Quadery
certifies that this is the approved version of the following dissertation:**

**HIGH POWER HIGH EFFICIENCY ELECTRON-HOLE AND
UNIPOLAR QUANTUM DOT LASERS**

Committee:

Dennis G. Deppe, Supervisor

Ray T. Chen

Leonard F. Register

Ananth Dodabalapur

Chih-Kang Ken Shih

**HIGH POWER HIGH EFFICIENCY ELECTRON-HOLE
AND UNIPOLAR QUANTUM DOT LASERS**

by

Sonia Quadery, B.Sc Honours ; M.Sc; M.S.E.

Dissertation

Presented to the Faculty of the Graduate School of

the University of Texas at Austin

in Partial Fulfillment

of the Requirements

for the Degree of

Doctor of Philosophy

The University of Texas at Austin

May 2007

Acknowledgements

First and foremost, I am grateful to Almighty Allah for graciously making it possible on my part to complete my Ph.D. dissertation.

It is a matter of great honor to thank my supervisor Dr. Dennis G. Deppe for his constant guidance and support and especially the wisdom he shared in this learning process.

I would like to acknowledge a special debt of gratitude to all my committee members for their valuable time and interest they have taken in my research work.

I wish to thank my colleagues: Dr. Gokhan Ozgur, Dr. Deepa Gazula and Dr. Hao Chen for their immeasurable help, support and friendship that count so much to me. Especial thanks to Dr. Sabine Freisem for growing the crystals for me.

The technical staff at the Microelectronics research center is greatly appreciated for making the cleanroom a safe place to work in. Administrative assistance of Ms. Jean Toll, Ms. Amy Pinkston and Ms. Melanie Gulick is deeply acknowledged.

Much is owed to Ms. Amy Perry at CREOL, UCF for making the much anticipated move from Austin to Orlando as smooth as possible.

I would like to thank all my friends in Austin who brought fresh air in my life after a long day in the lab.

As always, my heartfelt appreciation to my parents for their lifelong support and never-ending love. I am particularly indebted to my mother-in-law for her unconditional support and encouragement, she has been a great source of inspiration all along.

My deepest gratitude goes to my husband for always being there for me. This dissertation would not have been a reality without him.

And finally I would love to thank my baby Ayushi for putting up with her mommy and her dissertation and making every moment in my life meaningful.

**HIGH POWER HIGH EFFICIENCY ELECTRON-HOLE
AND UNIPOLAR QUANTUM DOT LASERS**

Publication No. _____

Sonia Quadery, Ph.D.
The University of Texas at Austin, 2007

Supervisor: Dennis G. Deppe

The goal of this research work is to develop and analyze Quantum Dot (QD) lasers aimed at improving high power performance which is crucial for numerous scientific, military and industrial applications. Fundamentally two dissimilar types of lasers are investigated: namely bipolar electron-hole laser and unipolar quantum cascade laser.

Planar quantum well (QW) laser diodes are already well-established as commercially available high power semiconductor lasers. However these lasers are unable to deliver power greater few 10's of watts due to reduction in efficiency at longer cavity lengths.

This limitation arises from inherent optical losses tied to the two-dimensional density of available states in QWs. A novel approach is proposed here to circumvent this limitation by introducing self-assembled QDs into the laser cavity which due to their delta-like discrete density of states promise to reduce the optical losses by at least an order of magnitude, hence allowing cavity length to increase proportionally. Detailed analysis based on harmonic oscillator model and solution at quasi-equilibrium condition reveal that total internal losses as low as 0.05 per cm^{-1} can be achieved in a QD laser enabling it to deliver 50 watts of power from each bar while maintaining efficiency close to 90%.

In order to take full advantage of the discrete atom-like behavior, it is also of utmost importance to reduce the inhomogeneous broadening of the dot distribution originating from size fluctuation. Experimental data of ultra narrow linewidth InAs quantum dots having linewidth of only 22 meV is presented. Research attempt has been taken to integrate these narrowly distributed dots into a workable structure. Preliminary data shows that these dots are extremely sensitive to the laser material which calls for careful optimization of the entire structure.

As for the unipolar QCL, it is shown that internal absorption caused by phonon emission of electrons in a planar quantum cascade laser represents a possible limitation to the maximum operating efficiency. Possibility of reducing this absorption is explored and it is optimistically asserted that introducing QDs into the gain stage of a QCL can eliminate this internal loss mechanism, thus greatly improving high power operating characteristics.

Table of Contents:

Chapter 1	Introduction and Outline.....	1
	1.1 Introduction	1
	1.2 Planar QW laser.....	2
	1.3 Motivation for high power QD laser.....	5
	1.3.1 High power high efficiency electro-hole QD laser.....	7
	1.3.2 High power CW Quantum Dot Cascade laser.....	8
	1.4 Organization of dissertation.....	10
Chapter 2	Self Assembled Quantum Dots.....	11
	2.1 MBE growth and formation of self assembled Quantum Dots.....	11
	2.2 Modeling of QD active region	13
	2.3 Material system and Photoluminescence	17
	2.4 Summary.....	20
Chapter 3	High power high efficiency QD diode laser performance analysis	21
	3.1 Optical losses in Semiconductor laser.....	21
	3.2 High power laser parameter analysis and optimization.....	24
	3.3 QD laser diode internal parameter analysis	26
	3.3.1 Cladding loss calculation.....	27
	3.3.2 Self-consistent solution of electron and hole Fermi functions.....	28
	3.4 Calculated results for electron-hole QD laser performance	32
	3.4.1 Cladding loss and confinement factor results.....	32
	3.4.2 Active region loss calculations.....	34
	3.4.3 Wall-plug efficiency characteristics.....	39

3.5 Summary.....	44
Chapter 4 Design, Device Processing and Characterization of QD diode lasers for high power applications.....	45
4.1 Design Considerations.....	45
4.1.1 Waveguide design and mode profiles.....	45
4.1.2 Choice of material for epi-structure.....	49
4.1.3 Device features.....	52
4.1.4 Packaging and heat management issues.....	53
4.2 Experiments and Results.....	54
4.2.1 Device fabrication and processing.....	54
4.2.2 Characterization of processed device.....	56
4.2.3 Experimental results.....	57
4.3 Summary	60
Chapter 5 Limitations of Planar Quantum Well Cascade Laser Model in high operating power range.....	61
5.1 Introduction.....	61
5.2 Basics of Quantum well cascade laser	62
5.3 Intersubband scattering and absorption mechanism in QWCL.....	64
5.4 Rate equation analysis.....	67
5.5 Calculated results and discussion.....	69
5.5.1 Impact of internal absorption on injection efficiency.....	72
5.5.2 Projected results for QD with longer τ_{32}	75
5.6 Conclusion.....	76
Chapter 6 Future direction and conclusion.....	76
Referenced cited in this dissertation.....	79
Vita.....	89

Chapter 1

Introduction and Outline

1.1 Introduction:

High power lasers are primarily classified as lasers that are capable of producing very high power optical output typically ranging from several watts to 100's of watts. Since the invention of lasers, high power lasers have become an essential component in numerous and diverse scientific and commercial fields. The major application areas include:

- Telecommunications as pump source for solid-state laser, fiber amplifiers and fiber lasers particularly in DWDM
- Military applications for example in LIDAR, infrared countermeasure etc.
- Industrial material processing such as soldering, welding, metal cutting, heat-treating etc.
- Biomedical applications in surgery, photodynamic therapy and other therapeutic applications
- Space applications such as in deep space data transmission systems
- Sensing and imaging, spectroscopy, large scale display and so on. [1,2,3,4]

In order to achieve superior performance, high power lasers should be capable of producing highly reliable bright light output. The most important criterion for high power laser is its efficiency which is described by its wall plug efficiency. Wall plug efficiency is basically the electrical-to-optical power conversion efficiency. Besides, other desirable features include temperature insensitivity, high reliability across the entire operating wavelength regime, small alpha factor which represents better beam quality etc.

Depending on what material is employed as the gain medium, there are wide varieties of high power lasers in use. Examples include solid state lasers, gas lasers, fiber laser and so on. But semiconductor heterostructure laser offers numerous merits and superior functionalities especially for high power operation. Semiconductor high power diode lasers are able to convert electrical power to optical power directly through electroinjection thus providing higher conversion efficiency, compactness of size, higher

optical gain, wide emission range which encompasses from visible to IR etc [1]. Also semiconductor lasers emitters can be integrated to form bar stacks and arrays so the optical output is multiplied to hundreds of watts. Therefore, bipolar Planar Quantum Well (QW) diode lasers have already found widespread use in high power applications. [2].

In mid and far IR ranges, another novel type of laser which is unipolar Quantum Well Cascade laser has been able to deliver good quality light output in watts regime thus replacing lead-salt based lasers in rapid succession [5]. However, currently the most severe constriction on achieving good emission power characteristics in QW lasers is caused by the internal loss within the devices themselves [6].

This limitation can be circumvented by introducing a fundamentally new type of gain material in the active region of the devices, namely Quantum Dot (QD) ensemble which promises to dramatically improve the high power operating characteristics of lasers.

1.2 Planar QW lasers:

The basic requirement to achieving high power output from a semiconductor laser is to keep the optical losses as low as possible [6]. Optical losses that are inherently present in the gain medium ultimately set the limit on how long a laser cavity can be made. When there is significant optical loss in the semiconductor material, the wallplug efficiency drops sharply with cavity length and with the cavity making shorter, the amount of collected power also decimates proportionally. This interplay between optical losses and efficiency will be addressed in details in chapter 3.

Before the advent of strained QW lasers, bulk semiconductor laser performance was limited by internal loss around 15-20 per cm due to huge free carrier absorption in the active region. Development of strained QW lasers not only reduced the losses by an order of magnitude but also yielded improvement in threshold current and temperature sensitivity thus paving the way towards high power operation [1]. Introducing strained InGaAs QWs in the active region resulted in improved material gain and extension of emission wavelength from near IR to mid IR. Owing to technological advancements

encompassing nearly two decades of research endeavor, planar QW laser technology is now very well established and QW diode lasers have become pervasive devices in high power application area.

Realizing the ever-increasing demand of high power lasers in both military and commercial sector, the US Department of Defense launched a program termed as SHEDS (super-high-efficiency diode sources) in 2003 to create diode lasers that have 80% wall-plug efficiency. Major improvement in high power planar QW lasers has already been made through interface bandgap engineering, waveguide adjustment, optimization of quantum-well designs combining the best materials etc. Here a prototype QW high power laser is shown in fig1.1 [4, 7].

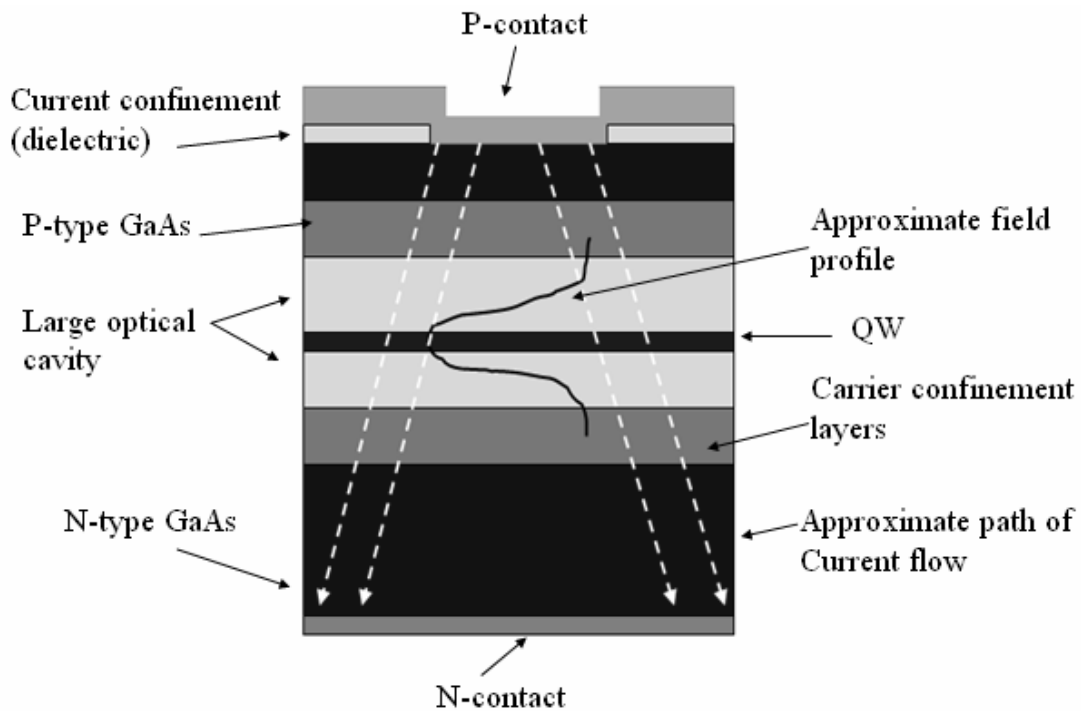


Figure 1.1 High power planar QW laser diode schematic

The strained QW layer is located in a large optical cavity which reduces the optical power density thus eliminating catastrophic optical damage to the end facets of the laser. The carrier confinement layer is separated from the waveguiding cavity to facilitate high carrier injection efficiency. A record 71% efficiency has been reported by employing this type of epitaxial structure with outputs as high as 22 CW. The lowest demonstrated internal optical loss in this kind of QW laser is 0.3 per cm so far [8].

Now we can examine the loss in efficiency in one of the best performed planar QW lasers in more details in figure 1.2 [2].

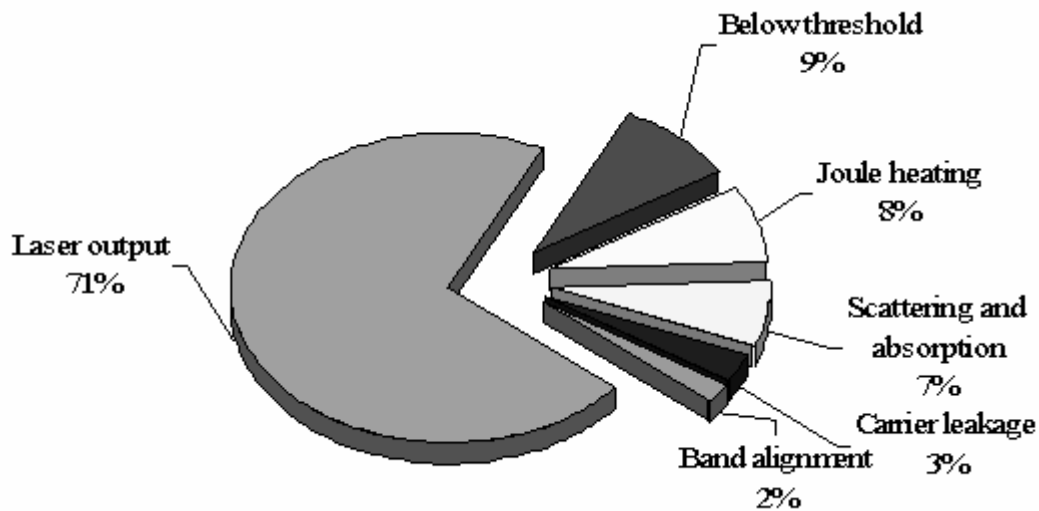


Figure 1.2 Loss components in a planar QW laser.

Before reaching threshold, 9% efficiency is lost since the injected carriers do not contribute in creating laser output. Inefficiency due to Joules heating originates from device series resistance and forward voltage across the p-n junction and worsens with higher drive current. Scattering and absorption losses arise due to imperfect crystal quality and free carrier absorption in the semiconductor material itself that accounts for the internal optical losses in the semiconductor. Leakage of carrier and subsequent recombination outside the active region causes addition photon loss. Build up of

heterojunction voltages due of misalignment of different heterobarrriers in the epitaxial layers also causes drop in efficiency. Optimization of band structure, doping profile and waveguide along with improvement in crystal growth quality can further increase the wallplug efficiency as mentioned earlier. However due to inherent losses in QW materials, there will be always certain amount of losses present in the devices, regardless of the advancement in planar QW technology. Therefore a novel approach ought to be sought to extend the laser operating regime towards higher wall plug efficiency.

1.3 Motivation for QD high power laser

Quantum Dot lasers offer numerous advantages over their quantum well counterparts due to three-dimensional confinement of charge comparable to its thermal de Broglie wavelength. Such quantum confinement of charges in the active region of the laser leads to delta-function like density of states resulting in atomic-like discrete energy level structure. This kind of modification of density of states directly contributes to dramatic reduction in transparency current density compared to a planar quantum well laser. For example, transparency current density of only 5 Amps/cm² can be achieved in a QD laser as opposed to at least 50 Amps/cm² in QW lasers. The most practical advantages associated with a QD laser are: ultra low threshold current density, higher optical gain and differential gain, high characteristic temperate T₀ giving temperature insensitive performance etc which all are very crucial especially in high operating power regime [9, 10, 11,12,13].

Figure 1.3 depicts simplified energy band structure in a QW and a QD to show the density of states in these two cases.

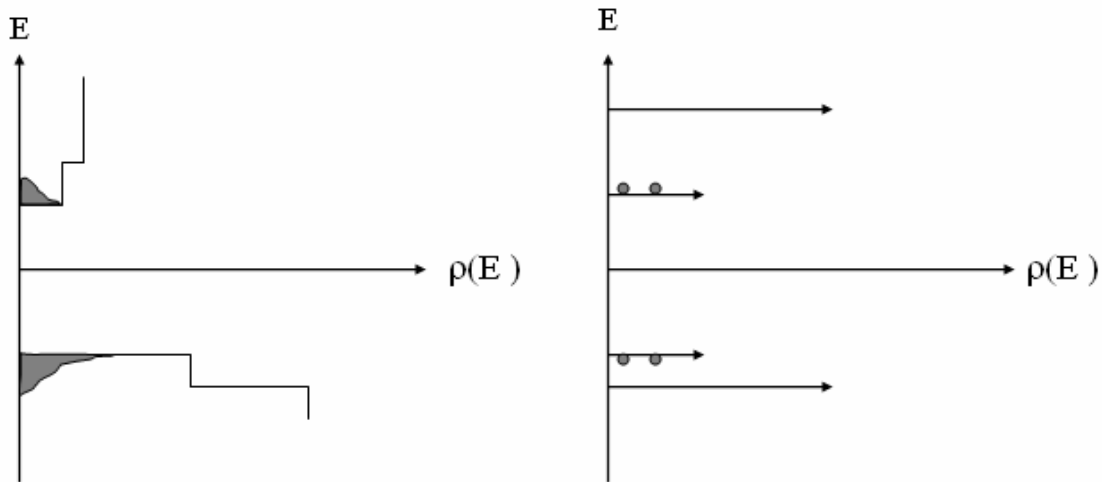


Figure 1.3 (a) Density of states in QW (b) Density of states in QD

In a planar QW, the density of states is a staircase like function so there is a continuous energy spectrum. This causes significant bandfilling and thermal smearing of populations in the subbands. Only a fraction of the carriers injected into the QW participate in lasing and as the temperature increases, more and more carriers are needed to be injected into the active region to sustain adequate gain for lasing. The minimum number of carriers to offset the losses in the QW active region, which is the transparency carrier density is expressed as:

$$N_{\text{trans,QW}} = \frac{4\pi m_{\text{red}}}{h^2} k_B T \dots\dots\dots(1.1)$$

Where m_{red} is the reduced mass, k_B is Boltzmann's constant, T is the active region temperature and h is Planck's constant. Owing to thermal broadening $k_B T$, the transparency carrier density goes up proportionally with temperature which increases the threshold current density. This higher threshold current causes junction temperature to rise, eventually resulting in a thermal feedback effect leading to device failure. For high power operation where 10's of amperes of current flows through the junction, this is a very severe phenomenon to be considered.

On the other hand, in an ideal QD material there is no such thermal broadening of carrier distribution. So taking into account twofold spin degeneracy, population inversion can be obtained when on an average each QD has one electron in excited state. Owing to discrete energy structure, maximum gain peak also remains unchanged and flat with respect to temperature.

1.3.1 High power high efficiency electron-hole QD laser:

Currently the high power operation of Planar QW lasers is limited to somewhat around 20 Watts from each laser emitter as stated in previous section. The chief source of limitation arises from physical size constriction of the laser ridges that originates from optical losses occurring in the semiconductor material itself. This loss is closely tied to the inherent properties of the active region and there can be a substantial decrease in internal loss through the reduction in transparency carrier density of the laser. In fact, all the major loss mechanisms that affect efficiency as described in previous section can be minimized through introducing three-dimensional charge quantization in QDs. The remarkable reduction in transparency carrier density directly leads to lower threshold density. The resistive loss which is I^2R greatly reduces due to lower operating current density as well. In this way, the wall plug efficiency in QD lasers can reach as high as 90% compared 70% in QW lasers. Furthermore, in optimizing laser performance, material gain is also of utmost importance since the threshold current density and modulation speed of laser strongly depends on gain. The most popular approach to achieve three dimensional carrier confinement is by MBE grown self-assembled III-V nanostructures embedded in epilayers. The optical gain of such self organized dots can be larger than that of QWs but ultimately the non-uniformity in dot size distribution sets limit on material gain. QWs grown on (110) orientation on GaAs wafers can improve the gain characteristics [2] but unlike QD laser, they will still suffer from high transparency and poor temperature characteristics. Moreover owing to lower antiguiding factor (also known as the alpha-factor) due to symmetric gain spectrum, QD lasers are expected to exhibit superior beam quality at higher power level compared to QW where filamentation

can occur otherwise. For all these attractive features, bipolar QD lasers hold tremendous possibilities to replace all other kind of bulky lasers eventually that are now used for near IR high power emission. The chief objective of this research work has been to analyze, model and design high power QD lasers. Also emphasis has been given to improve the material quality of self assembled QDs that will further enhance high power performance of lasers.

1.3.2 High power CW QD cascade lasers:

Quantum Cascade laser is a fundamentally new type of unipolar Mid/Far IR laser based on intersubband transition in QWs. Since its inception back in 1994, QCL have been substituting traditional lead-salt ($\text{Pb}_{1-x}\text{Sn}_x\text{Te}$ and $\text{PbS}_{1-x}\text{Se}_x$) based lasers that suffer from high Auger recombination and low efficiency. Planar QW QCLs have already found widespread use in chemical spectroscopy, biomedical sectors, as light detection and ranging (LIDAR) devices and infrared countermeasures [5,14]. In many of these cases, generation of high power continuous wave output is required. Currently the main limitation of QCLs is their inability in efficiently producing CW output at room temperature. It has been proposed in this research work that this efficiency of QCLs is severely affected by internal absorption in QW subbands due to longitudinal optical (LO) phonon emission. This LO phonon scattering predominates over the intersubband radiative transition of electrons. This inefficiency is analogous to the bipolar QW laser where the limitation arises from internal losses in the laser. Here internal absorption in QW subband also plays similar role.

On the other hand in QDs, owing to discrete energy levels this LO scattering mechanism is greatly reduced by creating so called phonon bottle neck as depicted in figure 1.4.

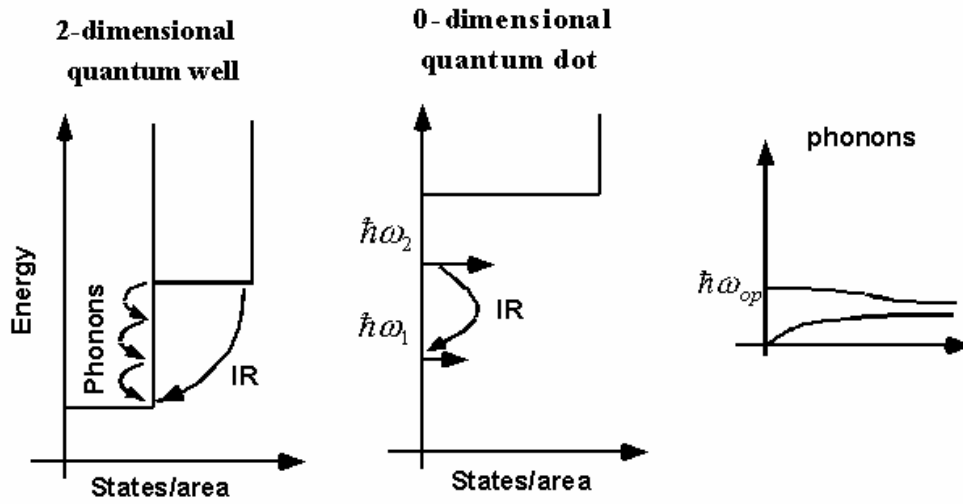


Figure 1.4 Phonon bottleneck in Quantum Dots

Typically the non-radiative phonon assisted relaxation time for electrons in excited states in QW subbands are on the order of picoseconds. In QDs this value can be several orders of magnitude higher. Therefore by introducing QDs as the active material in the cascaded gain structure, the internal absorption can be reduced to great extent with added benefits of lower threshold and less temperature sensitivity [15, 16]. The objective of present work is to gain a better understanding of the underlying physics of planar QCLs and analyze its high power performance and limitations which will lead to developing high power high efficiency Mid /Far IR lasers based on QD active material.

1.4 Organization of dissertation

We now review the organization and coverage of the thesis in sequence, chapter by chapter

Chapter 2 provides an overview of the structural, electronic and optical properties of III-V self-assembled Quantum Dots grown by Stranski Krastanow method in MBE system. The harmonic oscillator model of QDs is presented that helps in laying the theoretical framework for subsequent simulations of the QD lasers. Experimental results of ultra-low linewidth QD ensemble are shown which can remarkably improve QD laser gain characteristics.

Contents of chapter 3 aim at describing a reasonably complete picture of our present study focusing on achieving high efficiency high power operation using QD lasers. Various optical losses and their role in limiting high power output are outlined. Characteristic equations describing high power output and efficiency of semiconductor lasers are derived. The internal device parameters including active region loss, threshold current, forward voltage etc are computed based on self-consistent laser equation. Theoretically predicted results of QD lasers show remarkable improvement in wall plug efficiency through reduction in active region losses compared to its planar QW counterpart.

The critical design criteria such as waveguide design and material issues are addressed in Chapter 4. It also gives a detailed account of the fabrication sequences of QD laser aimed at combining the narrow linewidth QD ensembles in a laser cavity. Experimental results provide valuable feedback on epistructure optimization.

Chapter 5 is concerned with a fundamentally different type of unipolar laser, namely Quantum Cascade Laser. A considerable part of this chapter is devoted to showing that the inherent absorption mechanism is responsible for limiting high power output of such lasers. Alternatively QDs are shown to be a viable candidate in which this phonon assisted loss mechanism can be significantly diminished.

The concluding chapter i.e., chapter 6 presents the summary of research and future outlook for continuing this exciting field of research.

Chapter 2

Self Assembled Quantum Dots

Since first suggested in 1976 that three dimensional charge confinement can lead to dramatic improvement in laser performance, numerous techniques have been employed to create size quantization in semiconductor materials [[17]. The quantized dimensions should be comparable to thermal de Broglie wavelength which is on the order of nanometer scale, therefore it is very challenging to implement. Besides, since the QD ensemble is the active light emitting material, it should be comprised of very high quality defect free material. It was proposed back in 1982 by Arakawa that 3D Quantum confinement can be obtained in a two-dimensional QW by applying magnetic field to create the addition degree of quantization [9]. However from device point of view, it is more advantageous to combine the QDs within the active region of the laser. Several techniques such as using pre-patterned masked substrate, etching of lithographically defined layers etc have been employed to introduce QDs in semiconductor lasers in the past [18,19]. But these are basically ex-situ methods hence there is always possibility of contamination and moreover they are time consuming and complicated to due to multiple steps involved in the process.

From technological point of view, so far the most effective way to create three dimensional nanostructures is by self assembly of quantum dots in a highly stained material which is known as Stranski -Krastanow growth (also known as SK growth) [20]. In this in-situ mode of growth, QDs are spontaneously formed during epitaxial crystal growth. This type of formation was first observed by Goldstein [21].The following section will shed light on this technique of QD formation which has been employed in this research work.

2.1 MBE growth and formation of self assembled Quantum Dots:

The III-V self assembled quantum dots are grown in Molecular Beam Epitaxial (MBE) growth system. MBE systems are capable of depositing ultra high quality

materials with the layer thickness precision on the order of atomic scale. The source materials are thermally evaporated to form molecular fluxes that are deposited on the substrate in layer-by-layer fashion. Typically for III-V compound growth, the source materials are As, Ga, In Al, Be (as p dopant) and Si (as n dopant) [22].

In Stranski –Krastanow mode of growth, deposition of highly strained material on a crystalline matrix results in a pseudomorphic layer by layer growth until a critical thickness is reached where further deposition produces coalesced, defect free 3-D islands. This type of spontaneous growth occurs due to reduction of surface free energy of the strained material. Investigation shows that these types of islands have pyramidal shape as depicted in figure 2.1.

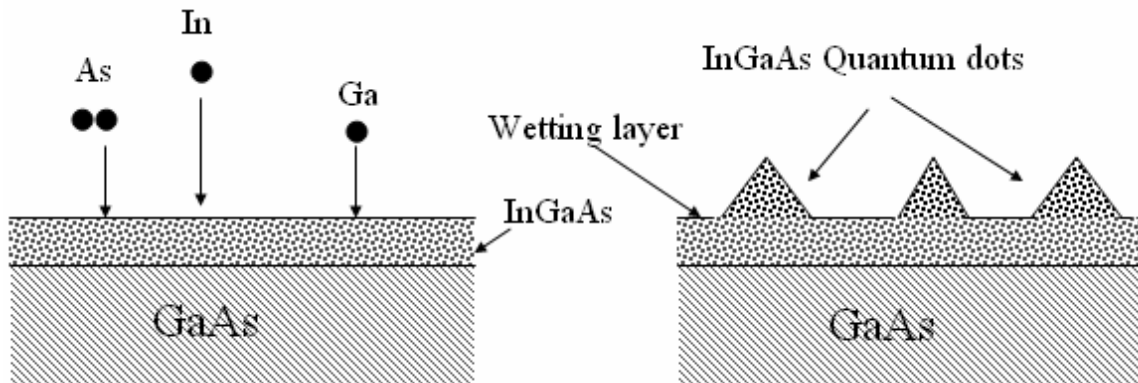


Figure 2.1 Stranski -Krastanow method of Quantum Dot formation

The most commonly used strained material combination is InAs on GaAs where the lattice mismatch is 7%. During initial growth, InAs forms smooth 2-D surface and once the critical thickness is reached, the extra InAs forms QD arrays while leaving the original planar thin layer behind [23,24,25,26]. This layer is known as the wetting layer. The thickness at which dot formation occurs is around 1.5 ML. There is a certain window within which these defect free dots occur. It has been found that upon depositing 3 ML

InAs on GaAs, additional materials tend to form clusters instead of coherent dot array [27].

The size and uniformity of QDs are strongly dominated by their growth condition such as growth rate, temperature and background As pressure. Since QDs are formed by material exchange via surface migration of adatoms, the mobility of adatoms is a crucial parameter in dot formation [28]. The adatom mobility is strongly dominated by substrate temperature and it also depends on deposition rate and background flux. There is an optimum temperature range at which dislocation free dots are formed. This range is normally between 490^o C and 530^o C. Higher temperature causes evaporation of dots out of the cap layer [29].

Besides, the quality of the QDs also depends on its surrounding material namely the underlying epilayer and the overgrown cap layer that covers it. For any device application it is desirable to have uniform arrays of quantum dots. The size distribution of the dots follows Gaussian distribution which is quantitatively characterized by the inhomogeneous linewidth in Photoluminescence (PL) spectrum. Usually the InAs dot sizes range from 20 nm to 50 nm and the densities are on the order of 10¹⁰ /sqcm to 10¹¹ /sqcm [27,30]. The typical values of inhomogeneous linewidth can be ~ 35 meV for a fairly uniform QD assembly.

2.2 Modeling of quantum dot active region:

Self organized QDs are extremely sophisticated objects whose electronic states largely depend on the surrounding material, the size and shape of the dots themselves and they are further influenced by the strain distribution around them [13]. The interesting fact is that the experimental PL data of self assembled QDs provide very useful information that can be employed to develop QD model quite accurately and determine its discrete electronic and hole states.

Figure 2.2 below shows a typical spontaneous spectrum of a QD edge emitting laser in which the ground, 1st and 2nd excited states appear at regular intervals [30, 31].

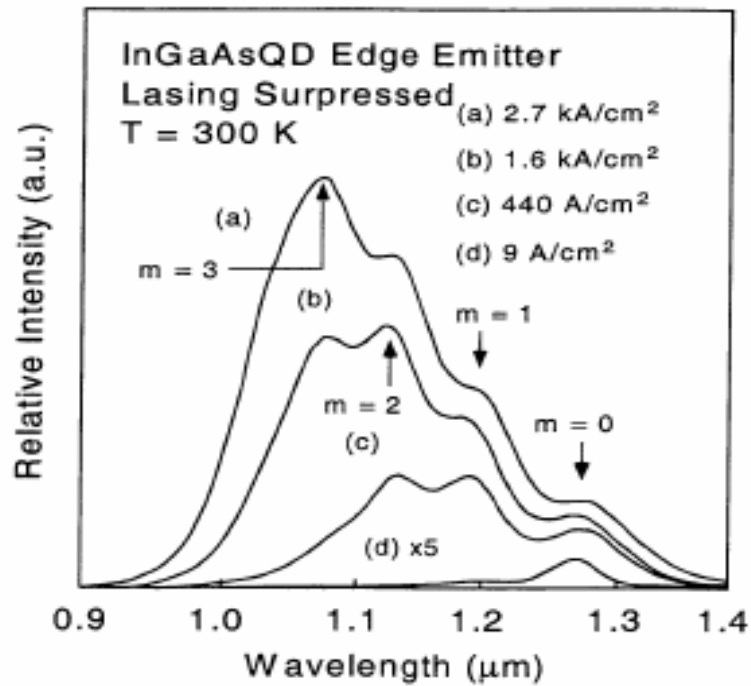


Figure 2.2 : Electroluminescence spontaneous spectra of InGaAs QDs .The four energy levels are labeled as “m”.

This phenomenon has close resemblance with that of a quantum-mechanical harmonic oscillator. The confinement potential in a simple harmonic oscillator takes up parabolic form in which its stationary states are equally spaced. Moreover there exists concentration gradient of In towards the center of the dot which can explain the parabolic shape of the potential [27, 32]. Furthermore, calculation of confining potential in QD by other groups also strengthens the parabolic potential theory [33]. The beauty of this model is that it is able to provide the exact solution of the electron and hole effective mass Hamiltonian. In an idealized QD, there are discrete electronic and hole states and a continuum of states generated from the wetting layer as depicted in figure 2.3 [30, 31, 34].

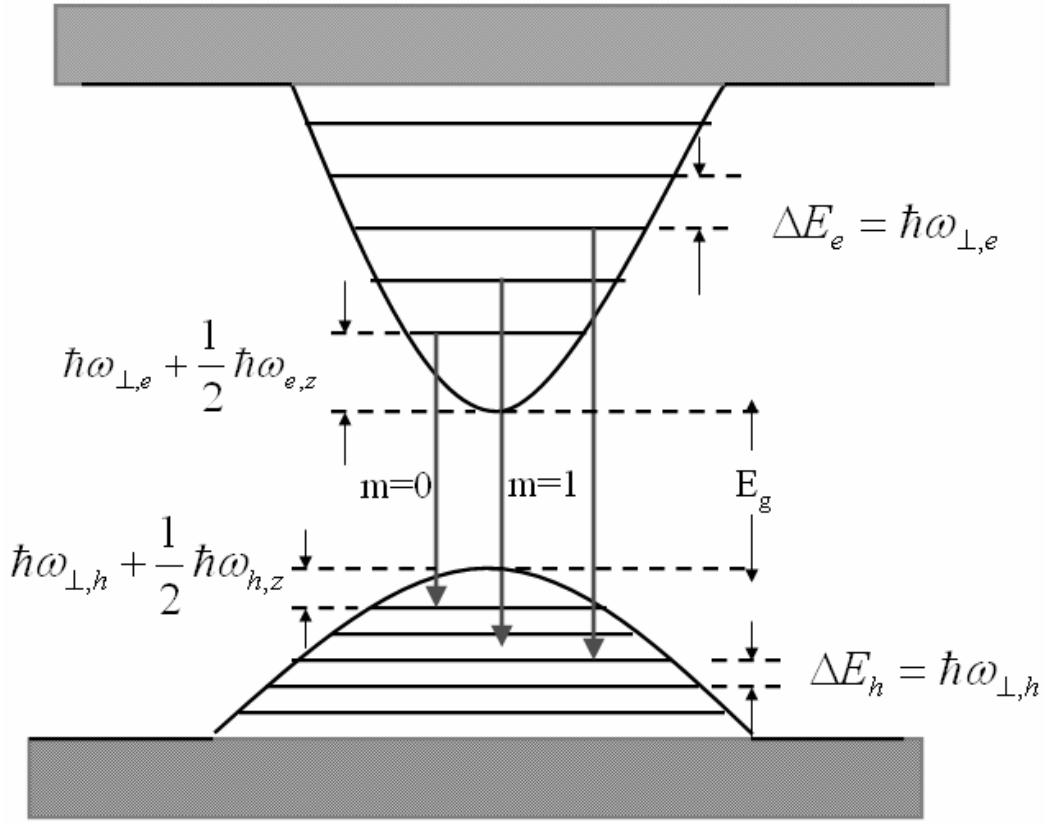


Figure 2.3 Energy structure in QD. Interband radiative transition is allowed exclusively between electron and hole pairs having same quantum number, m . Intraband transition is possible between any two levels.

The electronic (hole) energy level structure of the quantum dots can be numerically expressed by its Hamiltonian as follows:

$$\hat{H}_{e,h} = \frac{p_{e,h}^2}{2m_{e,h}} + V_{xy_{e,h}} + V_{z_{e,h}} \dots \dots \dots (2.1)$$

Where p , m and V are electron (hole) momentum, effective mass and confinement potential respectively. Here xy points to the lateral direction along the QD base edges and z is the direction along the height of QD.

The confinement potential is given in terms of the eigenfrequency, ω as:

$$V_{xy,e,h} = \frac{1}{2} m_{e,h} [\omega_{xy,e,h}^2 (x_{e,h}^2 + y_{e,h}^2)] \dots\dots\dots(2.2)$$

and

$$V_{z,e,h} = \frac{1}{2} m_{e,h} \omega_{z,e,h}^2 z_{e,h}^2 \dots\dots\dots(2.3)$$

Finally, the discrete energy levels are formulated as :

$$E_{m,e,h} = \hbar \omega_{xy,e,h} (m_x + m_y + 1) + \hbar \omega_{z,e,h} (m_z + \frac{1}{2}) \dots\dots\dots(2.4)$$

Here \hbar is Planck's constant divided by 2π ; m_x , m_y and m_z are positive integers that describe the degenerate energy eigenstates so that the m_{th} energy level E_m in the equation is represented by the combination of these integers i.e., $m = m_x + m_y + m_z$.

Usually the self assembled quantum dot height (z) is a few times smaller than the base diameter (xy) and the smaller the dimensions are, tighter is the quantum confinement. In other words, the energy level steps become smaller for bigger dimensions. Hence $\hbar \omega_z$ determines the energy difference between the wetting layer and ground state while the electron and hole spacings are given by $\hbar \omega_{xy}$. Since the electron effective mass is much smaller than that of the hole effective mass, it is expected that electron spacing $\hbar \omega_{e,xy}$ is several time bigger than hole spacing $\hbar \omega_{h,xy}$ [35,36]. This is also depicted in figure 2.3. As the confinement potential becomes deeper, the energy degeneracy becomes higher. For the sake of simplicity and also in compliance with measured AFM, the height to base arm ratio is approximated $\sim 1/2$. Typically a deep confinement potential can accommodate 5-6 discrete levels at best before the wetting layer continuum begins. This can be experimentally verified by measuring PL spectra which is also indicated in figure 2.2 Then based on this base to height ratio , the energy level degeneracies up to 5th levels are $s_0=2, s_1=4, s_2=8, s_3=12, s_4=18$ and $s_5=24$.

Because of the dipole selection rules, interband transition is allowed exclusively between electron and hole pairs having same quantum number, m which is the case of electron-hole bipolar diode laser. On other hand intraband transition is possible between any two electronic states that can occur in unipolar quantum cascade laser.

The ground state transition is given by:

$$E_0 = E_g + \frac{1}{2}\hbar\omega_{e,z} + \frac{1}{2}\hbar\omega_{h,z} \dots\dots\dots(2.5)$$

And excited state transitions are:

$$E_m = E_0 + m(\hbar\omega_{xy,e} + \hbar\omega_{xy,h}) \dots\dots\dots(2.6)$$

These discrete electronic (and hole) levels also influence the spontaneous lifetime for radiative transition τ_{sp} [37]. The reduced density of stated in an ideal QD is a delta function. But in an self-assembled QD array, accounting for the inhomogeneous linewidth $\Delta E = \hbar\Delta\omega$, the reduced density of state becomes [38]:

$$\rho_{red}(E) = 2\sqrt{\frac{\ln 2}{\pi}} \frac{N_{QD}}{\Delta E / 2} \sum_{m=0}^M s_m \cdot \exp[-\ln 2 \cdot \left\{ \frac{E - E_m}{\Delta E / 2} \right\}^2] \dots\dots\dots(2.7)$$

Here N_{QD} is the areal density of quantum dot ensemble. Due to the inhomogeneous linewidth, the spontaneous emission spectrum takes up Gaussian form. This reduced density state term is applied to calculate the optical gain of quantum dots that will be utilized in following chapter.

2.3 Material system and Photoluminescence:

Self-assembled quantum dot formation has been observed in numerous strained material systems. Specific examples on GaAs substrate include InAs/GaAs, InGaAs/GaAs, InAlAs/AlGaAs, InP/InGaP, just to name a few [28]. Among these, growth of InAs QDs on GaAs is one of the most well-established and widely exploited material systems since it favors rapid formation of Quantum dots due to huge lattice mismatch (7%). InAs QDs can be formed directly on GaAs or on InGaAs buffer layer and variation of buffer layer material alters dot property significantly including their energy states and surface density [27,39,40].

In present research work, InAs dots formed on GaAs substrate has been investigated in order to be incorporated into the QD laser cavity. InAs dots offers multitude of benefits that makes it a very promising material system for lasers. InAs dots have small lateral size and deep confinement potential hence the energy level spacing is wider that directly contributes to high characteristic temperature T_0 [27,30]. The deep localized potential also gives shorter emission wavelength which is useful for certain high power applications.

Photoluminescence spectroscopy is employed to study and characterize the InAs QD samples, this being a very powerful approach to characterize self assembled QD which are based on direct bandgap semiconductors materials. The full width half maximum of the spectra gives valuable information on dot inhomogeneous broadening. The peaks appearing in the spectrum correspond to the confined ground and excited states. In addition, the relative peak intensity of different samples can be compared to determine material quality.

Here we present the photoluminescence spectra of an InAs QD PL sample grown in our laboratory. The PL spectrum is exhibited in figure 2.4 along with the epistructure shown on inset.

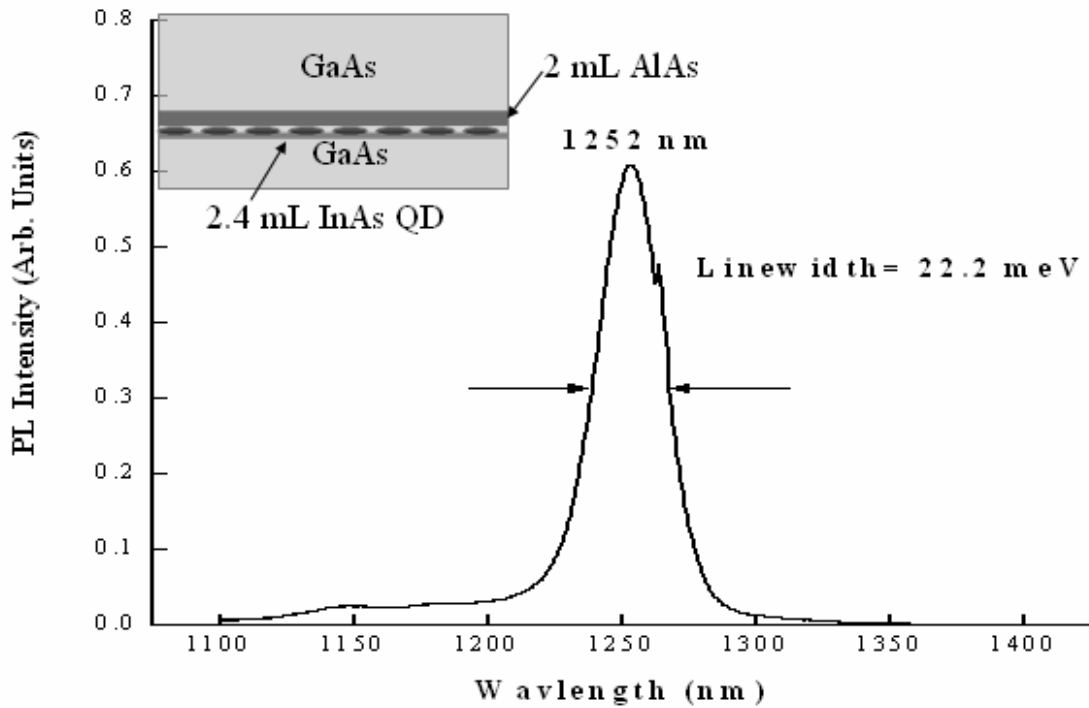


Figure 2.4 Photoluminescence spectra of narrow linewidth InAs Quantum Dots

The single quantum dot layers were grown at 510°C by continuous deposition of 2.4 monolayer of InAs on GaAs substrate. After dot formation, they were capped by a thin AlAs barrier. AlAs is believed to prevent interdiffusion and segregation of Indium; otherwise the local fluctuation in dot sizes can increase the inhomogeneous broadening [41]. The surface dot densities were measured around $3 \times 10^{10}/\text{cm}^2$. The density can be increased by vertically stacking the dot layers in the active region.

The PL sample was excited by CW He-Ne laser having emission at 632.8 nm at room temperature. The PL data reveals that the dots are very uniform possessing only 22 meV linewidth whereas typical values are above 35 meV. This narrow linewidth directly translates into higher optical gain as will be analyzed in following chapter. Owing to stronger confinement the gain peak is at 1252 nm which is shorter than InGaAs 1.3

micron dots. In specific high power applications such diode pumped solid state lasers; it is required to have emissions in 800-900 nm ranges. This wavelength range can be achieved by tailoring cap layer thickness and material composition and by incorporating Al into the InAs dots.

2.4 Summary:

Self assembled III-V Quantum dots formed by Stranski-Krastanow method is the most viable technique to incorporate semiconductor nanostructures into the epitaxial heterostructure laser. The dots formed in this way can be represented by a harmonic oscillator model. The clearly defined energy states in QDs with nearly equal spacings are in conformance with this model. Photoluminescence data of InAs quantum dot assembly grown on GaAs is presented having only 22 meV linewidth which is an unprecedented improvement over previously attained results.

Chapter 3

High Power High efficiency QD Diode Laser Performance Analysis

As pointed out in chapter one, the chief source of limitation in collecting power from planar QW laser arises from the inherent internal loss in the QW gain medium that in turn imposes length restriction on a laser cavity [6] . This chapter attempts to comprehensively analyze performance of a currently demonstrated high power QW laser and draw comparison with a proposed QD laser .The projected QD laser performance is simulated based on realistic parameters of QDs. The chapter begins with addressing various loss mechanisms in semiconductor with emphasis on internal loss. Laser parameters such as transparency current, threshold current density, forward voltage drop and modal gain for QD lasers are calculated in a self-consistent manner to evaluate the wall plug efficiency and optical power output that are achievable in this type of laser.

3.1 Optical losses in semiconductor laser:

Optical losses occurring in semiconductor can be broadly divided into mirror loss and internal loss .This is illustrated in figure 3.1. Mirror loss basically accounts for the portion of light that escapes from the cavity through its reflective facets of and is given by the following equation.

$$\alpha_m = \frac{1}{L} \ln\left(\frac{1}{\sqrt{R_F R_B}}\right) \dots\dots\dots(3.1)$$

In which α_m is the mirror loss, L is the length of the cavity and R_F and R_B are front and back reflectivities respectively. This clearly shows that by making the cavity longer, the threshold gain to offset losses can be made smaller; in other words the threshold current density can be reduced. For semiconductor /air interface the reflectivity values are typically around 0.3. But deposition of dielectric Bragg reflector (DBR) facet coatings can produce R_B reflectivity values of 95% or more and antireflective coating on front mirrors on the other hand can reduce the R_F values to 5% or less to facilitate more light output coupling.

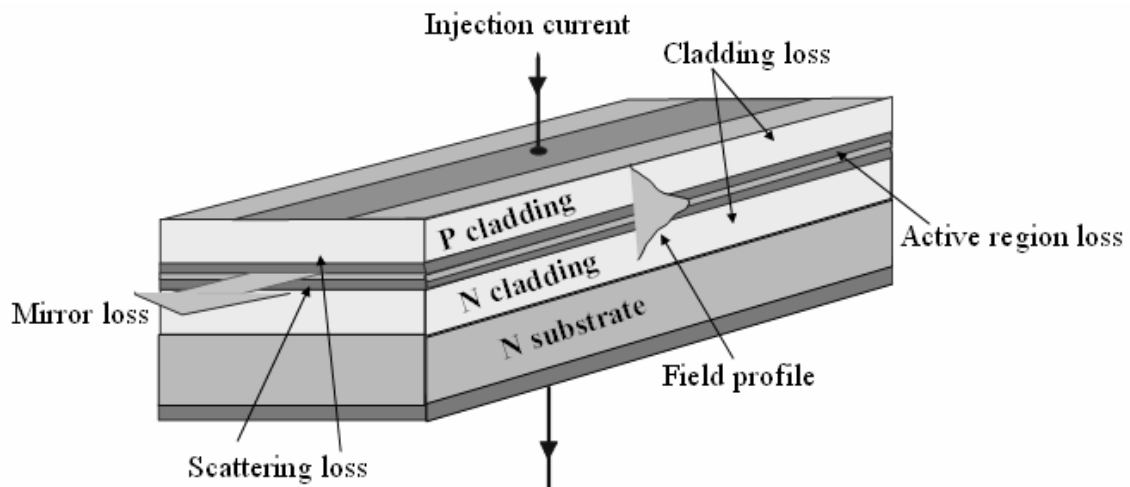


Figure 3.1 Optical losses in a semiconductor edge-emitting laser

The internal optical loss is a combination of several loss mechanisms as enumerated below:

- Free carrier absorption
- Scattering loss.

Free carrier absorption phenomenon occurs when either electron or hole in the same subband absorbs light and makes transition within the same band. This transition involves phonon for conservation of momentum. This type of absorption goes up with free carrier density. This is the dominant loss component in laser diodes. The free carrier

absorption is further made up of active region loss and cladding loss. The active region loss depends on the injected carrier density in other words the threshold current; hence it is largely dependent on the material properties of the laser. The cladding loss originates from the p and n doped claddings. These loss terms are expressed as:

$$\alpha_{active} = \frac{\Gamma_m}{\Delta z} (\sigma_e n_{e,th} + \sigma_h n_{h,th}) \dots\dots\dots(3.2)$$

$$\alpha_{cladding} = \Gamma_{ncladding} \sigma_e n_{dope} + \Gamma_{pcladding} \sigma_h p_{dope} \dots\dots\dots(3.3)$$

Here Γ 's are the optical field overlap integral which will be discussed in the next chapter in waveguide design issues. Δz is the active region thickness which is used to normalize modal overlap. The σ terms are free carrier scattering cross-sections that vary with semiconductor material and wavelength. The scattering cross-section for holes in GaAs is several times bigger than that for electrons [6,42].

The active region loss expression indicates that absorption loss can be greatly minimized by lowering the threshold carrier density in the active region, $n_{e,th}$ ($n_{h,th}$) which is achieved by keeping the transparency carrier density at a minimum level. Besides, careful optimization of doping and waveguide profiles will further reduce the internal loss. However, there is always a trade-off in such optimization since reducing modal overlap causes modal gain to drop and lightly doped waveguide introduces higher resistive paths for injected carriers. Considering these factors, the best solution would be to keep the transparency carrier as low as possible. Quantum dots have a clear advantage over QWs in this regard as we have discussed in chapter 1.

Lastly, scattering losses come from inhomogeneity of the material and heterointerfaces in the epistucture. This can be made negligible by improving crystal growth quality and judicious choice of material. The appropriate material choices for waveguide and claddings will be further discussed in the next chapter.

3.2 High power laser parameter analysis and optimization

Wall –plug efficiency is the single most important parameter to characterize high power laser performance and this parameter is largely dependent on the internal loss of the device. The excess power which is not converted into output light produces wasted heat. It is a daunting task to remove wasted haste from the active region which calls for expensive and bulky heat removal systems and cooling assembly. On the other hand, unless efficiently removed, this heat causes the junction temperature to rise and ultimately shorten lifetime of the laser [2].

Now we shall focus on wall-plug efficiency characteristics of an edge emitting laser and its dependence on basic device parameters. The wall plug efficiency, η_{wp} of an edge-emitting laser is given as the product of internal quantum efficiency η_i , optical extraction efficiency η_{opt} and electrical conversion efficiency, η_{elec} as follows:

$$\eta_{wp} = \frac{P_0}{P_i} = \eta_i \times \eta_{opt} \times \eta_{elec} \dots \dots \dots (3.4)$$

Though shown as separate terms, all the efficiency terms are interrelated. Trying to optimize any one of these causes the other to change for example by reducing doping in the cladding region and broadening the waveguide will bring improvement in optical efficiency. However, lightly doped claddings will introduce larger series resistance which will cause electrical efficiency to degrade and broader waveguides will cause η_i to drop [43]. Hence careful optimization is required to maximize wall-plug efficiency. However, in semiconductor lasers, since the carrier density is pinned above threshold, the η_i value can approach 100%.

The wall plug efficiency expression can be further elaborated as:

$$\eta_{wp} = \eta_i \times \frac{\ln\left(\frac{1}{R_F}\right)}{2\alpha_i L + \ln\left(\frac{1}{R_F R_B}\right)} \times \frac{h\nu_{ph}(I - I_{Th})}{q(I^2 R_s + IV_f)} = \eta_i \times \frac{\ln\left(\frac{1}{R_F}\right)}{2\alpha_i L + \ln\left(\frac{1}{R_F R_B}\right)} \times \frac{h\nu_{ph}(J - J_{Th})}{q(J^2 \rho_s + JV_f)} \dots \dots \dots (3.5)$$

Then the output power is expressed as:

$$P_o = \eta_i \times \frac{\ln\left(\frac{1}{R_F}\right)}{2\alpha_i L + \ln\left(\frac{1}{R_F R_B}\right)} \times \frac{h\nu_{ph}(I - I_{Th})}{q} = \eta_i \times \frac{\ln\left(\frac{1}{R_F}\right)}{2\alpha_i L + \ln\left(\frac{1}{R_F R_B}\right)} \times \frac{h\nu_{ph}(J - J_{Th})WL}{q} \dots \dots \dots (3.6)$$

In these equations, input power $P_i = WL(J^2\rho_s + JV_F)$, L is the laser cavity length, W is the stripe width , $h\nu_{ph}/q$ is the voltage related to the radiated photon energy, V_F is the forward voltage at the p-n junction active region with $V_F \geq h\nu_{ph}/q$, I is the electrical current, I_{th} is the threshold current, and R_s is the electrical series resistance and α_i is the internal loss. In the second expression on the right in (3.5) and (3.6), the wall-plug efficiency is expressed in terms of the current density J, current density threshold J_{th} , and the electrical contact sheet resistance ρ_s , because these parameters are more fundamental to the semiconductor materials.

The maximum obtainable wall plug efficiency is formulated as:

$$\eta_{wp,max} = \eta_i \times \frac{\ln\left(\frac{1}{R_F}\right)}{2\alpha_i L + \ln\left(\frac{1}{R_F R_B}\right)} \times \frac{\frac{h\nu_{ph}}{q\rho_s J_{Th}}}{\left(1 + \sqrt{1 + \frac{V_F}{\rho_s J_{Th}}}\right)^2} \dots \dots \dots (3.7)$$

Which occurs at the current density $J = J_{Th} \left(1 + \sqrt{\frac{V_F}{\rho_s J_{Th}} + 1}\right) \dots \dots \dots (3.8)$

Hence the maximum wallplug efficiency depends on both operating power level as well as intrinsic device parameters. It is clearly evident that the product $\alpha_i L$ sets limit on $\eta_{wp,max}$ and there is always a drop in maximum wallplug efficiency associated with an increase of cavity length [28]. On the other hand, as expressed in equation (3.6), the amount of output power level increases linearly with cavity length L. Therefore to

achieve high power while maintaining high efficiency we need to increase the length of the cavity. Decreasing α_i allows us to implement edge-emitters as long as few cm's without sacrificing wall-plug efficiency.

In typical quantum well lasers having losses of ~2-3 per cm, it is almost impossible to maintain high power output as the efficiency drops significantly. As this efficiency reduction is tied to the internal loss in QW laser, it cannot be entirely eliminated since a minimum number of carriers i.e. transparency carriers have to be present in the active region to achieve optical gain for lasing.

Moreover by L is making longer, the threshold gain to lase g_{Th} and the series resistance R_s also become smaller as explicitly shown in following relation :

$$g_{Th} = \alpha_i + \frac{1}{L} \ln\left(\sqrt{\frac{1}{R_F R_B}}\right) \dots \dots \dots (3.9)$$

$$R_s = \frac{\rho_s}{WL} \dots \dots \dots (3.10)$$

This also implies reduction in forward voltage to establish threshold gain, threshold current density and bias current thus yielding higher electrical efficiency and reliability as well. In following section we shall analyze performance of a QD laser and show that through reduction in internal loss, the cavity length can be increased by at least an order of magnitude thus enhancing the efficiency to a record level.

3.3 Quantum Dot diode laser internal parameter analysis:

This section is devoted to analyzing the operating characteristics of a bipolar QD laser. The basic device parameters such as internal loss α_i , forward voltage drop across the active region V_F , threshold current density J_{Th} etc are solved in a self-consistent manner in order to simulate high power performance of a quantum dot laser.

The quantum dot laser model is based on quasi-equilibrium distribution of carriers in quantum dots. This model is fairly accurate at room temperature and at higher temperature where the escape rate of thermally activated carriers is much higher than that

of the radiative lifetime in the dots [12,13] .In quasi-equilibrium condition, it is believed that due to extremely rapid thermalization (typically on the order of picosecond), the electrons and holes can be approximated as occupying thermal distributions in their respective energy levels in QDs. Hence the occupation probability of electrons and holes can be described by Fermi distribution and quasi-Fermi levels determined by external pumping level. In most of the practical applications, the active region temperature of high power lasers becomes substantially higher than room temperature due to large current density which validates this approach of quasi-equilibrium model.

We began our analysis by determining the internal losses of a QD laser in an accurate fashion. Assuming that scattering loss can be made practically negligible for reasons explained later, the remaining cladding loss and active region losses are evaluated as follows.

3.3.1 Cladding loss calculation:

Recalling the expression for cladding layer loss as given in equation (3.3), it is obvious that the losses in cladding are proportional to the optical field overlap in the cladding region. For a given doping level, the cladding loss therefore is totally determined by transverse mode profile in waveguide. The mode profile solution is based on a simple numerical procedure that calculates effective indices in a multilayer slab waveguide by applying boundary conditions for electric and magnetic fields in each layer using Maxwell's equations. For given thicknesses and refractive indices, the boundary conditions in successive layers result in a series of 2×2 transfer matrices and the effective indexes of corresponding to the guided modes that exclusively satisfy the matrix equation set [44]. Once the effective index is known, the electric field intensity along the transverse direction as well as the percentage of field overlaps in each layer can be computed.

The fundamental mode profile is used to calculate the cladding region overlaps in a given waveguide structure. The waveguiding layer is typically GaAs and the cladding regions are 70%AlGaAs though various other material compositions will be discussed in next chapter. The InAs QD layers embedded in the waveguide are assumed to be a thin

sheet (typically 60 Angstrom) in order to calculate the field profile. The mode profile solution also yields confinement factor in the active region which is utilized in calculating optical gain and active region loss. However the quantum dot surface density is later taken into account for gain calculation which then gives correct expression in spite of this approximation of thin sheet of InAs.

3.3.2 Self consistent solution of electron and hole Fermi functions:

The self consistent solution of electron and hole Fermi function is a very robust method of obtaining fundamental device parameters such as threshold current, internal loss and operating voltage. This calculation is founded on charge neutrality condition [12, 30] and threshold condition for lasing .As the electron and hole concentrations are found from the quasi-Fermi levels E_{Fe} and E_{Fh} respectively, therefore these energy terms contain the connection between threshold gain g_0 and its dependence on the electron and hole concentrations. The electron(n) and hole(p) concentrations in an individual QD are expressed in terms of Fermi functions f_{m_e} and f_{m_h} respectively as:

$$n = \sum_{m_e}^{M_e} f_{m_e} = \sum_{m_e=0}^{M_e} \frac{s_{m_e}}{\exp[(E_{m_e} - E_{F_e})/kT] + 1} \dots\dots\dots(3.11)$$

$$p = \sum_{m_h}^{M_h} (1 - f_{m_h}) = \sum_{m_h=0}^{M_h} \frac{s_{m_h}}{\exp[-(E_{m_h} - E_{F_h})/kT] + 1} \dots\dots\dots(3.12)$$

Where the summation runs over all the degenerate discrete levels in the quantum dot having degeneracy of s_m .The electron and hole levels are equally spaced, the difference between successive levels being ΔE_e and ΔE_h respectively. Hence the electron and hole concentrations can be further expressed in terms of ground ($m=0$) level Fermi functions f_{0e} and f_{0h} as follows:

$$n = \sum_{m_e=0}^{M_e} \frac{S_{m_e}}{\exp(m_e \Delta E_e / kT) \left(\frac{1}{f_{0e}} - 1 \right) + 1} \dots\dots\dots(3.13)$$

$$p = \sum_{m_h=0}^{M_h} \frac{S_{m_h}}{\exp(-m_h \Delta E_h / kT) \left(\frac{1}{f_{0h}} - 1 \right)^{-1} + 1} \dots\dots\dots(3.14)$$

Where, Fermi functions for the ground states are

$$f_{0e} = \frac{1}{\exp[(E_{0e} - E_{F_e}) / kT] + 1} \dots\dots\dots(3.15)$$

$$f_{0h} = \frac{1}{\exp[(E_{0h} - E_{F_h}) / kT] + 1} \dots\dots\dots(3.16)$$

In a QD having deep confining potential, charge neutrality condition is maintained in the QD active region where radiative transition occurs .In such case, the influence of wetting layer can be ignored too [12]. Then the charge neutrality condition relates the electron, hole and any other charge concentration existing in the active region in such a way that the opposite charges balance each other. For the case of simplicity we assume that only free carriers exist in the active region (disregarding unintentional doping) so that the charge neutrality condition can be expressed as:

$$n = p \dots\dots\dots(3.17)$$

where n and p expressions are given in the equations above. This relationship holds true especially when injected carriers are efficiently being captured in active region.

Therefore the quasi Fermi level separation ($E_{Fe} - E_{Fh}$) is determined by charge neutrality condition which in turn controls the carrier occupancies in discrete energy levels.

The ground state modal gain equals to the optical losses at threshold and for edge-emitting laser at a particular lasing mode. The threshold gain is defined as [38,45]:

$$g_{oTh} = \frac{\left(\frac{\lambda_0}{n}\right)^2}{\tau_{sp}} \sqrt{\frac{\ln 2}{\pi}} \frac{\Gamma_m}{\Delta z \Delta \omega} 2N_{QD} (f_{0eTh} - f_{0hTh}) \dots\dots\dots(3.18)$$

Here λ_0 is the free space wavelength, n is the refractive index in the cavity, τ_{sp} is the QD radiative spontaneous lifetime, $\Gamma_m/\Delta z$ is the modal confinement factor normalized by the active region thickness, $\Delta\omega$ is the inhomogeneous broadening of energy spectrum having Gaussian width, N_{QD} is the surface dot density, and $(f_{0eTh} - f_{0hTh})$ is the inversion factor for electron-hole energy levels. The value of τ_{sp} is given by [46]:

$$\tau_{sp} = \frac{3\pi\epsilon_0 c^3 \hbar}{n\omega_0^3 q^2 |\vec{d}|^2} \dots\dots\dots(3.19)$$

Where ϵ_0 is the permittivity of free space, c is the speed of light in vacuum, ω_0 is the transition frequency, q is the electronic charge and $|\vec{d}|$ is the dipole.

At lasing threshold,

$$g_{oTh} = \frac{1}{L} \ln \frac{1}{\sqrt{R_F R_B}} + \alpha_{clad} + \alpha_{active} \dots\dots\dots(3.20)$$

Since active region loss α_{active} depends on the carrier concentration in the active region, therefore at threshold it can be expressed as:

$$\alpha_{active} = \frac{\Gamma_m}{\Delta z} (\sigma_n n_{Th} + \sigma_p p_{Th}) N_{QD} \dots\dots\dots(3.21)$$

In which n_{Th} and p_{Th} are threshold electron and hole carrier densities respectively. At threshold condition, Equation (3.17) and equation (3.20) can be solved simultaneously to find the threshold carrier densities. The solutions will also give results for active region loss.

The threshold current density then can be related to electron and hole occupation probability and spontaneous emission rate as follows [30,38]:

$$J_{Th} = \frac{qN_{QD}}{\tau_{sp}} \sum_{m_e=0}^{M_e} \frac{s_m}{\frac{e^{(E_{m_e} - E_{F_e,Th})}}{kT} + 1} \cdot \left(1 - \frac{1}{\frac{e^{(E_{m_h} - E_{F_h,Th})}}{kT} + 1} \right) \dots\dots(3.22)$$

In which the selection rule for radiative transition is also taken into account.

Finally, since the forward voltage drop is actually the electron and hole quasi Fermi level separation required to establish positive gain in the active region, thus it can be solved once the Fermi functions values are obtained as shown below:

$$V_f = (E_{F_{e,Th}} - E_{F_{h,Th}}) / q \dots\dots\dots(3.23)$$

The additional voltage drop above transparency, $(V_F - hv_{ph}/q)$ is required to offset the optical losses and maintain gain in the active region .The expressions derived here for active region loss, threshold current density and forward voltage can be used to model the high power efficiency and light output of QD lasers. The simulated results are presented in following section.

3.4 Calculated results

In this section we investigate the high power QD diode laser wall plug efficiency characteristics for various laser designs that impact the internal device parameters such as active region losses, threshold current, voltage drop etc. How basic QD parameters such as dot density and hole level spacings affect the device performance are addressed. On the other hand, the influence of waveguide design parameters on laser characteristics is also explored. It is readily seen, that for a number of optimized design, the QD laser can exhibit unprecedented improvement of wall plug efficiency through huge enhancement in cavity length. Comparative results of a best performed QW laser and a simulated QD laser will be presented based on optimized data as calculated.

3.4.1 Cladding loss and Confinement factor results: The cladding losses and confinement factor by and large depend on the thickness of the waveguiding region. Typically the design rule is to maximize the optical confinement factor in the active region. But it comes at a cost of increased free carrier absorption in the active region and scattering losses due to large optical field overlap. For a given waveguide and cladding material composition, there is a certain thickness range at which the maximum overlap occurs in the epi-growth direction. Here we simulate the optical losses based on device data of our present 1.3 micron QD lasers that are designed for maximum confinement. The cladding losses can be calculated accurately for a known waveguide structure and the scattering losses can be obtained from experimentally measured internal loss values. Based on that, the scattering loss values can then be extrapolated for different waveguide thicknesses.

The device structure consists of two stack InAs QD layers embedded in a 2200 Å thick 5% AlGaAs waveguide and surrounded by 85% AlGaAs cladding layers on both sides having doping levels = $5 \times 10^{17} \text{ cm}^{-3}$ [27]. The normalized confinement factor is calculated as $3.4 \times 10^{-6}/\text{m}$. The absorption cross-section values used are $\sigma_n = 3 \times 10^{-18} \text{ cm}^2$ and $\sigma_p = 7 \times 10^{-18} \text{ cm}^2$ which are fairly accurate for GaAs and 0.98 micron wavelength [6]. The total internal loss was measured 1.8 per cm in which cladding loss was calculated 0.46 per cm.

Based on the threshold current density, the active region loss is estimated at 0.075 per cm so that the major contribution comes from scattering loss=1.26 per cm. The plot in figure 3.2 shows that the confinement factor peaks at around 2200 \AA and deviates on both side.

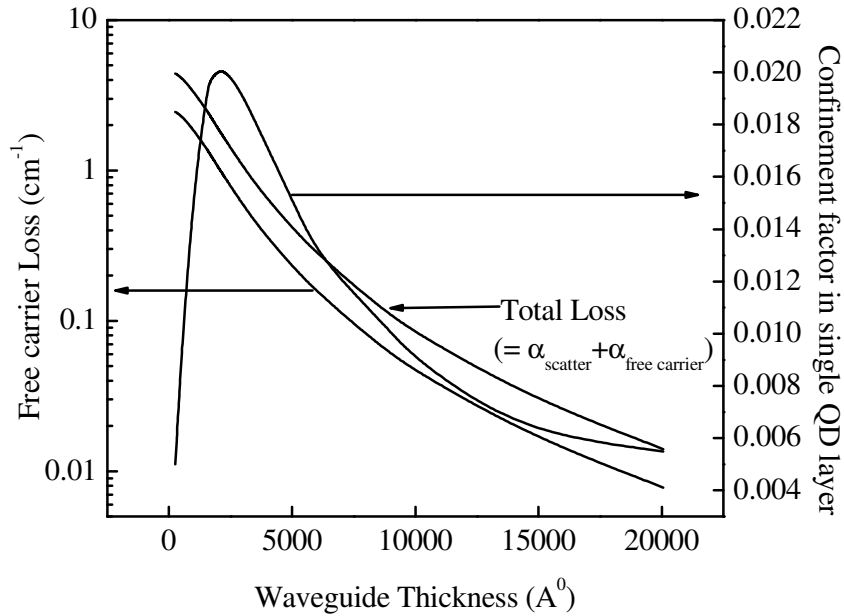


Figure 3.2 Optical losses and confinement factor vs. waveguide thickness

In the same plot it is evident that when the waveguide is made broader, the cladding and scattering losses drop quite faster compared to the confinement factor. For example, at waveguide thickness =7500 \AA the confinement factor drops to 57% of the maximum confinement value but on the other hand the cladding overlaps are reduced by a factor of 4. It is clearly evident from the plot that as we make the waveguide thicker, the cladding losses substantially go down and can reach values as low as 0.05 per cm. By further reducing doping levels in cladding, these losses can be made close to zero. This kind of waveguide design issues will be discussed in details in next chapter. The scattering losses which we assume to come mostly from cladding/core heterointerfaces also drop

significantly as the mode is spread out in wider waveguide. Wider waveguide also simultaneously forces the modal confinement to drop which means the gain coefficient becomes smaller. This effect can be compensated by making the QD arrays more uniform. Besides as long as the lasers operate well below ground state gain saturation, the reduction in modal gain does not pose any problem considering that the threshold current density is also small in QD lasers.

3.4.2 Active region loss calculations: The close hole spacing in QDs compared to electron spacing are diagnosed as the major limiting factor in QD laser performance. The electron level spacings can be as wide as 80-90 meV whereas the hole level spacing are only around 10 meV [35,36,47]. In such cases, the carriers in hole levels are thermally smeared out among a number of levels that forces the injected carriers into individual quantum dot to go up to maintain sufficient population in the ground state to lase [47,48]. This ultimately increases threshold current, forward voltage drop and most importantly active region loss. The hole spacings also determine the occupancy probability of carriers in higher energy levels.

The following plot in figure 3.3 shows the number of electrons (holes) in each dot versus the occupied energy levels for hole spacings, ΔE_h of 10, 20 and 50 meV. The QD characteristic parameters used in this calculation were: $\lambda=0.98$ micron, QD density $N_{QD} = 3 \times 10^{10} / \text{cm}^2$ (single stack), electron spacing $\Delta E_e = 90$ meV, inhomogeneous linewidth $\hbar\Delta\omega = 30$ meV, radiative lifetime $\tau_{sp} = 800$ pS and the height/base ratio (h/D) is taken as $1/2$ for degeneracy calculations. The waveguide consisted of 1 micron thick GaAs core and 70% AlGaAs cladding with doping = $5 \times 10^{17} \text{cm}^{-3}$ yielding cladding loss of 0.025 per cm and modal confinement of $1.7 \times 10^6 / \text{cm}$.

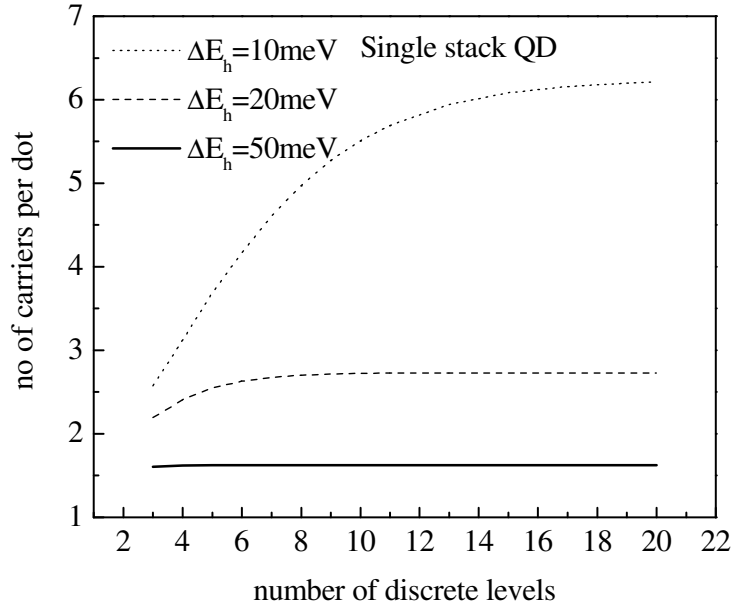


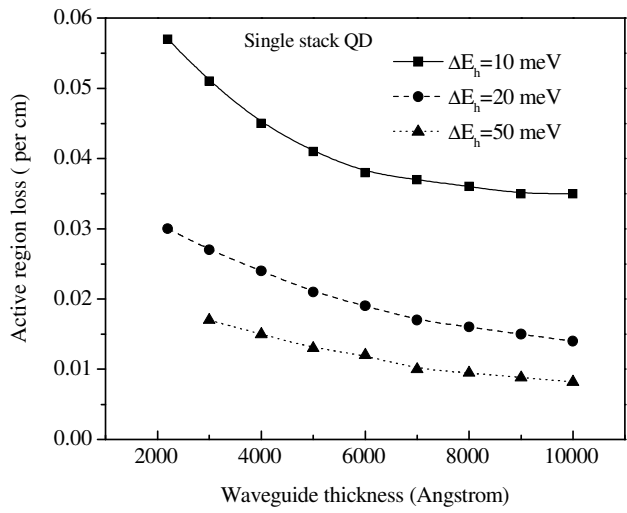
Figure 3.3 Carrier occupancy in dots for different hole level spacings

The plot shows that when the hole level is as large as 50 meV, only the ground states become occupied containing one pair of e-h per dot on average. However, for 10 meV spacings, this number goes up to 6 e-h pair per dot and regardless of the spacing, the carrier numbers tend to saturate around 7 kT that accommodates around 12 discrete hole levels in the worst case. Usually for deep confinement potential, the barrier height between ground state and wetting layer is also close to this value. Hence for further calculation we include up to 12 discrete levels to examine the effect of hole spacings on other parameters. It may be mentioned that by controlling growth condition and tailoring dot material, wider hole spacing can be obtained. The other attractive scheme is to introduce p dopants in the QDs which has already proven to improve differential gain and characteristic temperature T_0 in p-doped QD lasers [27,48] .

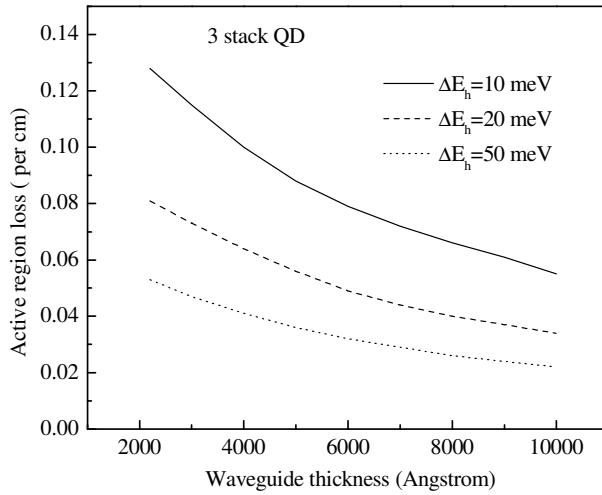
We also examine the effect of dot density on the device performance. The dot density can be increased by vertically stacking Quantum dot layer separated by a thin GaAs spacer.

Here we present plots in figure 3.4 showing waveguide thickness dependence on active region loss. The effect of increasing dot density is also taken into account. The curves are generated for three distinct cases of hole level spacings namely 10, 20 and 50 meV. The cavity length is chosen to be 1 cm and R_F and R_B values are 0.05 and 0.95 respectively. Here we notice in 3.4(a) and (b) that the active region losses do not change too much with waveguide thicknesses but the total internal loss changes dramatically as evident in 3.4(c). However the active region loss improves quite a bit as the hole level spacings are made wider as expected. Also in case of three stack QD, the active region losses have around threefold increase compared to single stack.

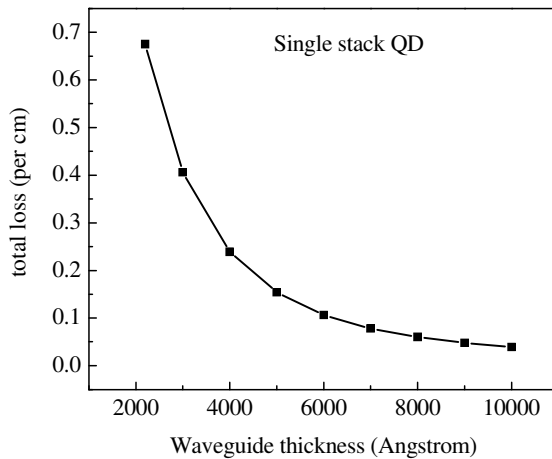
This increment can be explained due to enhancement of transparency carriers in the active region in triple stack QDs. This also contributes to higher threshold current density in three stack QD layers. However the forward voltage drop V_F goes up slightly with increasing waveguide thicknesses (not shown) due to the smaller gain coefficient value that forces the quasi Fermi separation to become larger.



(a)



(b)



(c)

Figure 3.4 Active region loss for different waveguide thicknesses having (a) 1 stack QD and (b) triple stack QD and (c) total losses vs. waveguide thickness for same structure.

The following plot shows the dependence of cavity length on active region losses calculated for 1 micron thick waveguide in case of 10, 20 and 50 meV hole spacings of single and triple stacked QDs again.

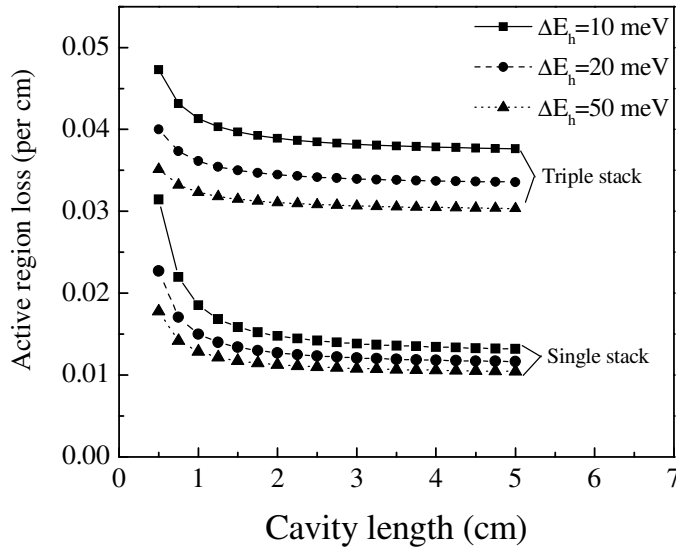


Figure 3.5 Cavity length dependence on active region losses

As the cavity length increases, we expect the threshold gain to go down due to lower mirror losses and this behavior is exactly reflected in the plot. We again find that in case of single stack widely spaced hole levels, the loss terms are at minimum level. Upon comparing figures 3.4 and 3.5 we also notice that the major loss component is loss due to cladding loss with the exception of 10meV triple stack QDs in which the active region loss exceeds the cladding losses at thicknesses above 6000 Angstrom.

On the other hand, due to gain enhancement the forward voltage drop across the active region improves slightly as we increase the dot density . Later we are going to inspect the overall performance of single and triple stack dot layers lasers and the impact

of active region loss, threshold current and voltage drop on maximum obtainable wall-plug efficiency. The following table compares these parameters for single and triple stack QD layers having 1 micron thick waveguide and 1 cm long cavity. The hole spacings are taken as 20 meV.

Table 3.1

Parameters	Single stack	Triple stack
Active region loss	0.014 per cm	0.034 per cm
Threshold current density	3.5 Amps/sqcm	7.7 Amps/sqcm
Forward voltage drop	1.295 V	1.275 V

3.4.3 Wall plug efficiency characteristics: Now we investigate the effect of waveguide thickness on maximum obtainable wall plug efficiency for the same cavity and waveguide configuration with the exception of lighter doping at $5 \times 10^{16} \text{ cm}^{-3}$. As seen from the plot below, the maximum efficiency peaks at almost 93% at thickness around 7000 Angstrom. For thinner waveguides, the efficiency is limited by internal loss (mostly cladding losses) which drops with increasing thickness. However beyond 7000 Angstrom the efficiency rolls off due to increasing forward voltage drop with waveguide thickness which is also more pronounced for low doped cladding and shorter cavity lengths. The waveguide design issues will be more closely examined in following chapter.

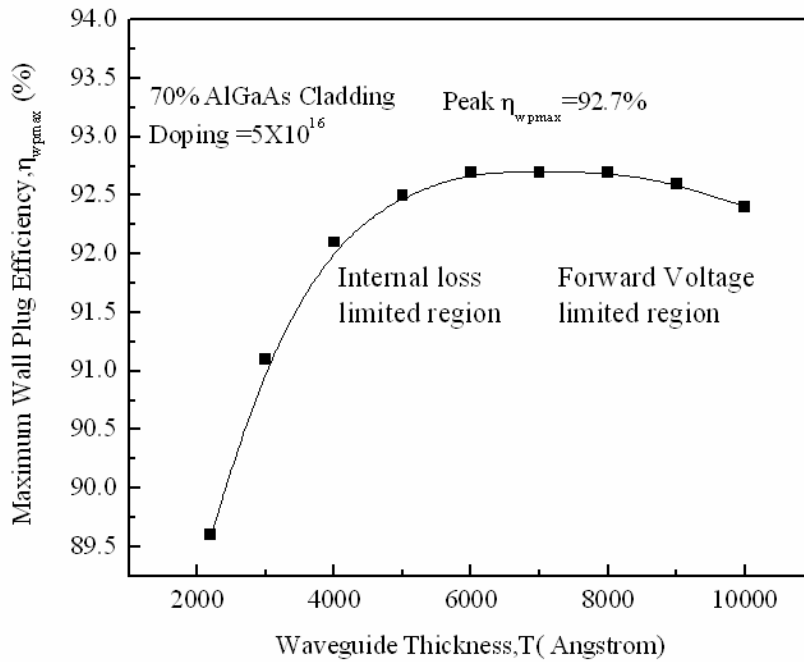


Figure 3.6 Complex behavior of maximum wall plug efficiency due to interplay between internal loss and forward voltage drop

The influence of p doping the QD has been taken into account as well. Introducing p dopants helps in reducing the transparency density but on the other hand the active region losses go up due to the free carrier absorption by the dopants themselves. As a result we don't see any considerable improvement on wall plug efficiency as shown in table 3.2 The waveguide thickness is 6000 Angstroms in this calculation.

Table:3.2

Acceptors per dot	Active region loss	Maximum Wall plug efficiency
0	0.0075 per cm	88.75%
2	0.0086 per cm	88.52%
5	0.015 per cm	87.36%

So it is more plausible to employ widely spaced hole levels instead of p doping the QDs when internal loss is the limiting factor rather than the differential gain in device performance [27,47].

The key contribution in improving high power performance is a due to longer cavity lengths in QD lasers therefore we compute the optimum cavity length values at which maximum power conversion efficiency can be reached. First of all, in order to choose a range of suitable waveguide thicknesses, the wallplug efficiency of a 1 cm long cavity for different waveguide thicknesses is calculated .This is shown in figure 3.7.

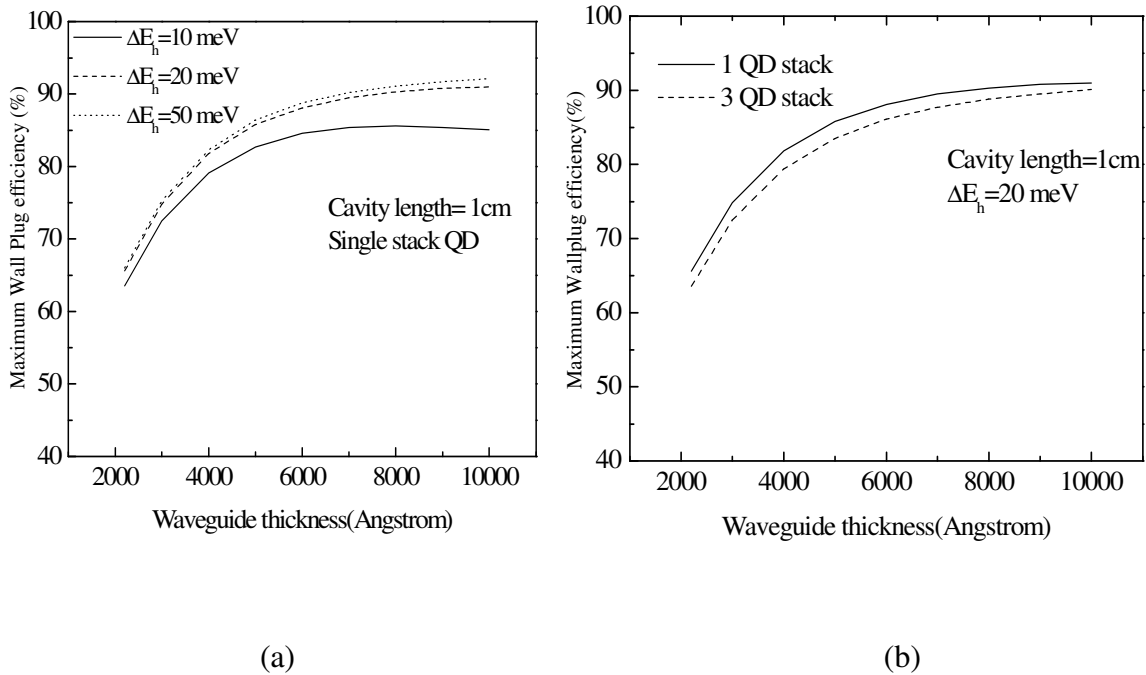


Figure 3.7 (a) Maximum wall plug efficiency variation with waveguide thickness for a single stack QD active region .Plot (b) shows that the efficiency values are slightly better for single stacks compared to triple stacks.

The device parameters used in this calculation are : stripe width = 100 micron, sheet resistance= 7.5×10^{-5} ohm-sqcm and internal efficiency is assumed 100%.Plot (a) shows

that the wall plug efficiency can reach a very high value which is around 90% for 20meV hole spacing in a single stack QD laser. The efficiencies improve considerably for thicker waveguides ($>7000 \text{ \AA}$). It is evident from plot (b) that the efficiency is better for single stack quantum dots than triple stack dots inspite of smaller gain. The hole spacing is chosen 20 meV again in the later plot. This is very important to note since usually it is believed that stacking QDs can bring improvement in high power characteristics [28].

The maximum achievable wall plug efficiency for particular cavity lengths is then plotted out for 1 micron thick waveguide using 20 meV hole level spacing. The peak value approaches nearly 93% at cavity length~1.5 cm which is almost fivefold increase in length compared to typical length values for QW lasers.

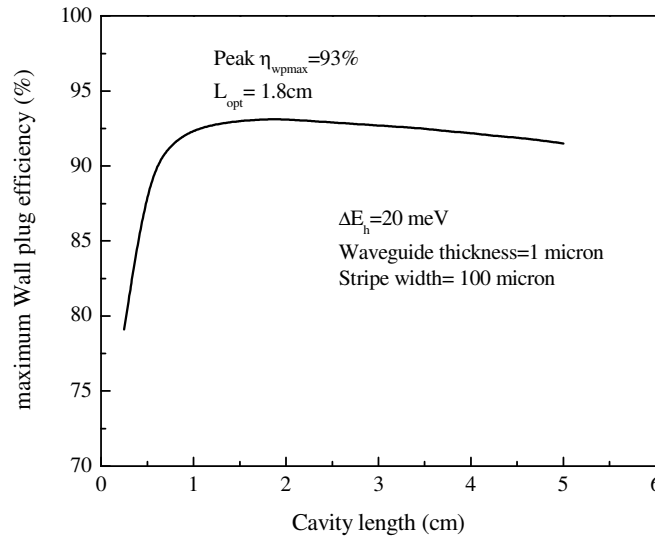


Figure 3.8 Maximum wall plug efficiency as a function of cavity length shows that QD lasers can be several cm long while maintaining efficiencies higher than 90%

Finally we present projected result of a QD high power laser based on internal loss, optimized cavity length and a reasonable threshold current density and compare side by side to that of a planar QW laser which has been recently demonstrated [8]. The key parameters are given in table 3.3 .

Table 3.3

Parameter	QW	QD
Cavity length (L)	0.3 cm	1.5 cm
Internal Loss (α_i)	0.34 per cm	0.05 per cm
Threshold current density(J_{Th})	90 Amps/sqcm	20 Amps/sqcm

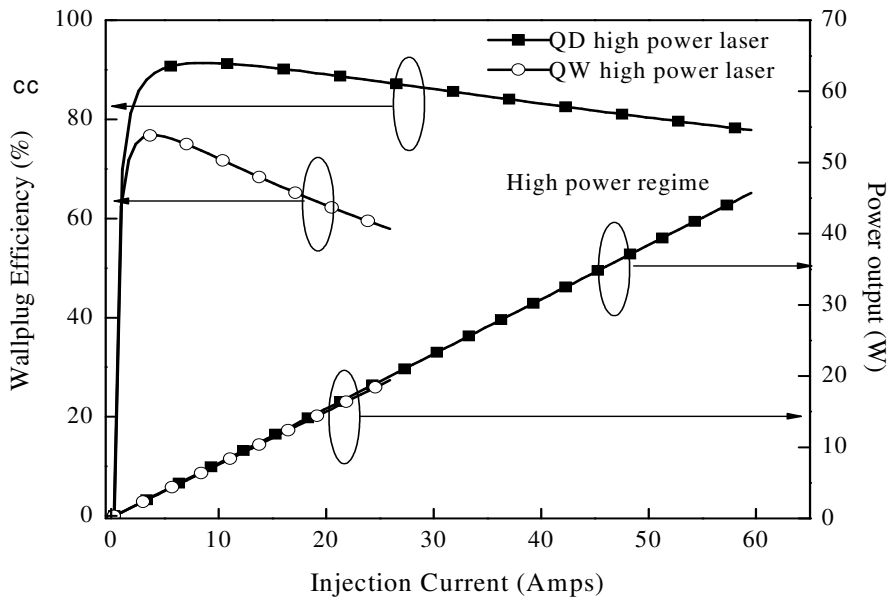


Figure 3.9 Projected high power operation of QDs compared to QW high power lasers. Dotted lines show limited power and efficiency in QW lasers.

The other parameters (η_i , R_F, R_B , λ, ρ_s etc) are identical in both cases. As expected, the operating range for QD laser is remarkably extended towards the high power end while maintaining wall plug efficiency as high as 90% or more. On the other hand the theoretical maximum efficiency for QW lasers is around 75% for $L=3$ mm at drive current of 4 Amps and sharply drops above that. By the time the power output reaches 16 Watts, the efficiency drops to only 50% while in case of QD lasers the conversion efficiency is above 80% even when the output power level reaches close to 50 Watts.

We have not yet considered the effect of reduction of injection efficiency in broader waveguide which can affect the high power results. However through band engineering and proper waveguide designs this effect can be kept small [2, 43].

3.5 Summary: The high power quantum dot laser operating characteristics has been presented in this chapter. Brief description of optical losses encountered in a semiconductor is given with emphasis on free carrier absorption in active region. Equations to analyze high power performance in a semiconductor lasers are formulated. The device parameters for a QD laser are calculated in a self-consistent fashion based on quasi equilibrium model and charge neutrality condition. Besides waveguide parameters such as mode profile and cladding layer losses are computed using Maxwell's wave equations for electric and magnetic field. It has been discovered that the closely spaced hole levels can severely degrade QD performance. However by engineering the dot growth and material, the hole level spacings can be made wide enough to overcome this problem. The dot density also affects the efficiency characteristics of the laser. It has been concluded that the QD laser will best perform in high power regime when a single stack QD layer having widely spaced hole levels are embedded in a broad waveguide. In this kind of configuration, the optimized cavity length can be as long as several centimeters without sacrificing wall plug efficiency. In these long cavity low loss QD lasers, the wall plug efficiencies can reach an unprecedented level of greater than 90% which is impossible to achieve in a planar QW laser.

Chapter 4

Design, Device Processing and Characterization of QD Diode Lasers for High Power Application

For high power operating range of QD laser, there are several design criteria that should be taken seriously; starting with waveguide design, then fabrication and lastly proper mounting techniques for characterization since at high drive current there is significant device heating that may cause junction failure. We shall focus on all these design issues in this chapter. Besides preliminary device results will be presented that provide valuable insight into how to improve high power characteristic of QD lasers.

4.1 Design considerations: As we have discussed in previous chapter, broad waveguides are considered as very promising candidates to keep internal losses at ultra low level. But it comes with a cost of several demerits for example evolution of higher transverse order modes, somewhat inferior injection efficiency etc [8,43,49]. In section 4.1.1 we propose several schemes to combat these detrimental effects.

From material point of view, it is important to combine a number of design rules in realizing the laser epistucture; choice of appropriate material system, optimization of doping level etc to name a few. These topics will be addressed in section 4.1.2. On the other hand from device point of view, we need to consider several critical aspects such as capability of withstanding high current, ease of fabrication that can provide rapid turn out for feedback to the epistucture growth experiments and so on. These issues will be discussed in section 4.1.3 and 4.1.4.

4.1.1. Waveguide design and mode profiles:

The optical confinement factor is the key parameter to describe a waveguide. It gives the fraction of optical power contained in the active region and is expressed as [30]:

$$\Gamma = \frac{\int n_{active} E_{active}^2}{\int n_{active} E_{active}^2 + \int n_{guiding} E_{guiding}^2 + \int n_{cladding} E_{cladding}^2} \dots\dots\dots(4.1)$$

On the other hand, in order to estimate cladding losses, we need to consider the cladding layer field overlap which is given as:

$$\Gamma = \frac{\int n_{cladding} E_{cladding}^2}{\int n_{active} E_{active}^2 + \int n_{guiding} E_{guiding}^2 + \int n_{cladding} E_{cladding}^2} \dots\dots\dots(4.2)$$

Here n's are the refractive indices of relevant layers and E's are the electric field intensities. Upon comparing these two expressions, it is apparent that trying to maximize one causes the other to degrade. So it calls for careful optimization of waveguide thicknesses, material combination, placement of active region, doping density in the claddings and so forth.

Here we present graphical solution of a waveguide mode profile in figure 4.1 having two different waveguide thicknesses namely 2200Å and 7500 Å that illustrates the consequence of broadening the waveguide. The transverse field profiles were calculated at λ=1.25 micron for 5% AlGaAs waveguide and 85% AlGaAs cladding having single stack InAs Quantum dot active region layers. As the waveguide thickness becomes 7500 Å, very little amount of evanescent mode tail remains in the cladding region thus giving ultra low cladding losses. Besides, broader waveguide has other benefits too for example due to smaller optical density the catastrophic optical mirror damage (COMD) which is identified as one of most common reason for high power semiconductor laser failure; can be avoided [2,50,51]

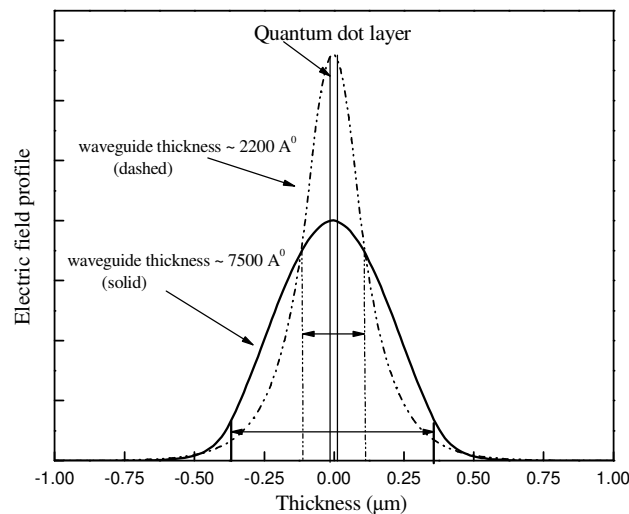


Figure 4.1 Transverse electric field profiles of two different waveguide thicknesses

However recalling the waveguide equation for the number of modes that are supported in a planar waveguide:

$$N_{Modes} \cong \text{Int}\left(\frac{k_0 d \sqrt{n_{guiding}^2 - n_{cladding}^2}}{\pi}\right) \dots\dots\dots(4.3)$$

We see that upon increasing waveguide thickness d, the number of modes also goes up linearly. Here k_0 is the free space wave number. In order to prevent higher order modes from lasing an ingenious scheme can be followed [8] .By positioning the active region asymmetrically in the waveguide region, the multimode lasing can be inhibited as shown in figure 4.2 .

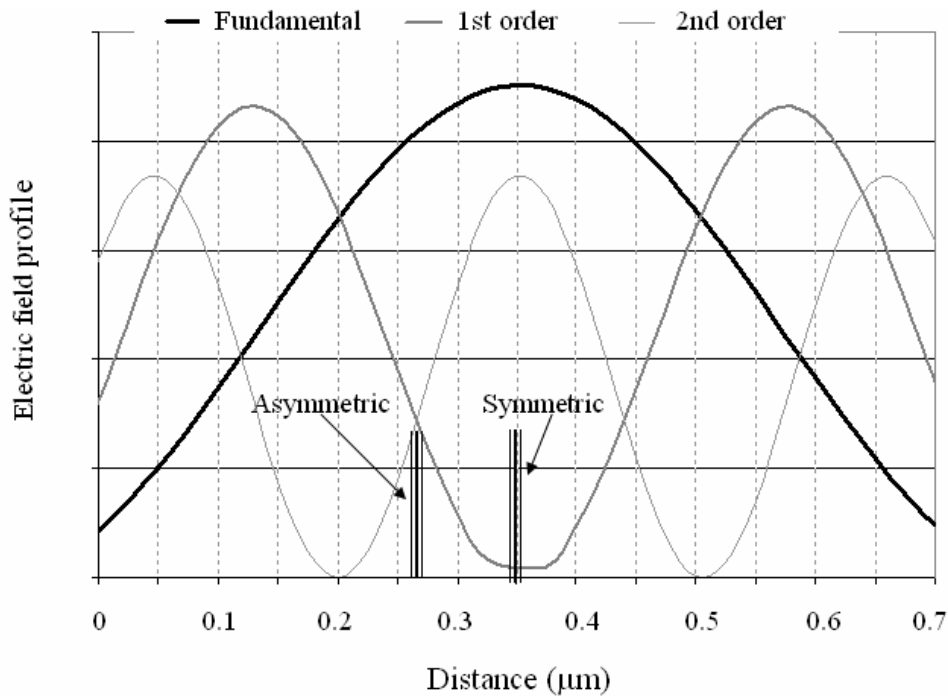


Figure 4.2 Asymmetric positioning of active region prevents lasing of higher order modes

The mode profiles shown here were calculated for 7000 Å GaAs waveguide having 85% AlGaAs cladding layers. When the quantum dot layer is placed in the middle where maximum confinement for fundamental mode occurs, it also coincided

with the 2nd order mode. However as we shift the position of the dot layers approximately 1000 \AA away from the center, the higher order modes are discriminated, thus prevented from lasing. We calculate that in this way the modal overlap reduces from $2.26 \times 10^6/\text{m}$ to $2.1 \times 10^6/\text{m}$ which is only around 7% reduction in confinement factor.

Another drawback of broadened waveguide is that the injection efficiency suffers at higher current level [49]. Since the hole mobility is almost an order magnitude lower than the electron mobility in AlGaAs, therefore by placing the active region closer to p interface can mitigate this effect. Besides injection efficiency can be further improved by grading the cladding/guiding layer interfaces,.

We also consider the possibility of employing an asymmetric waveguide structure with lower Al composition on n cladding and higher Al composition on p cladding. The benefit of this kind of structure is that it pushes the mode deeper into the n side and as the electron absorption coefficient is smaller than that of holes, the cladding losses can be further cut down as shown schematically in figure 4.3.

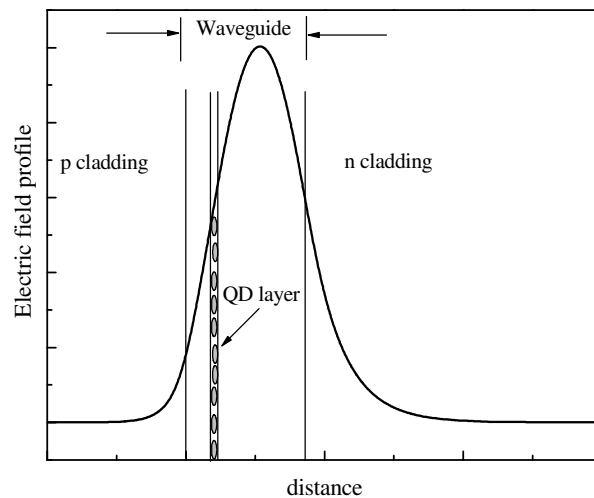


Figure 4.3 Asymmetric waveguide structure having different Al composition on p and n sides

Moreover, the higher order cut off thickness in this kind of asymmetric waveguide also decreases since the number of mode depends on the difference of cladding –waveguide refractive indices difference. This is depicted in figure 4.4.

Therefore this kind of asymmetric waveguide also gives us freedom to place the QD in any convenient position.

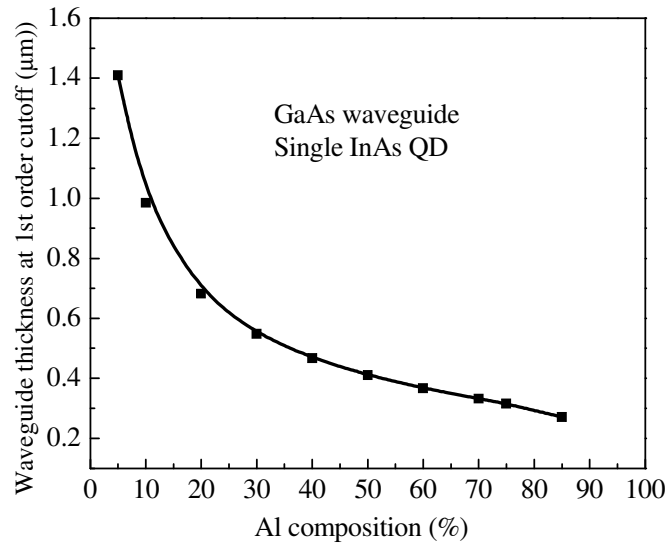


Figure 4.4 1st order cutoff thickness vs. Al composition

4.1.2 Choice of material for epistucture: A typical epitaxially grown structure of a QD diode laser relevant to our discussion is presented here for reference. The active region consists of two stack InAs QDs. The sample is grown on n doped substrate. The cladding materials are high Al containing AlGaAs layers and the waveguiding layer is GaAs. In case of multiple stacks of QD, there is a thin GaAs spacer in between the QD layers. The topmost layer is a heavily p doped (usually 10^{19} cm^{-3}) contact layer.

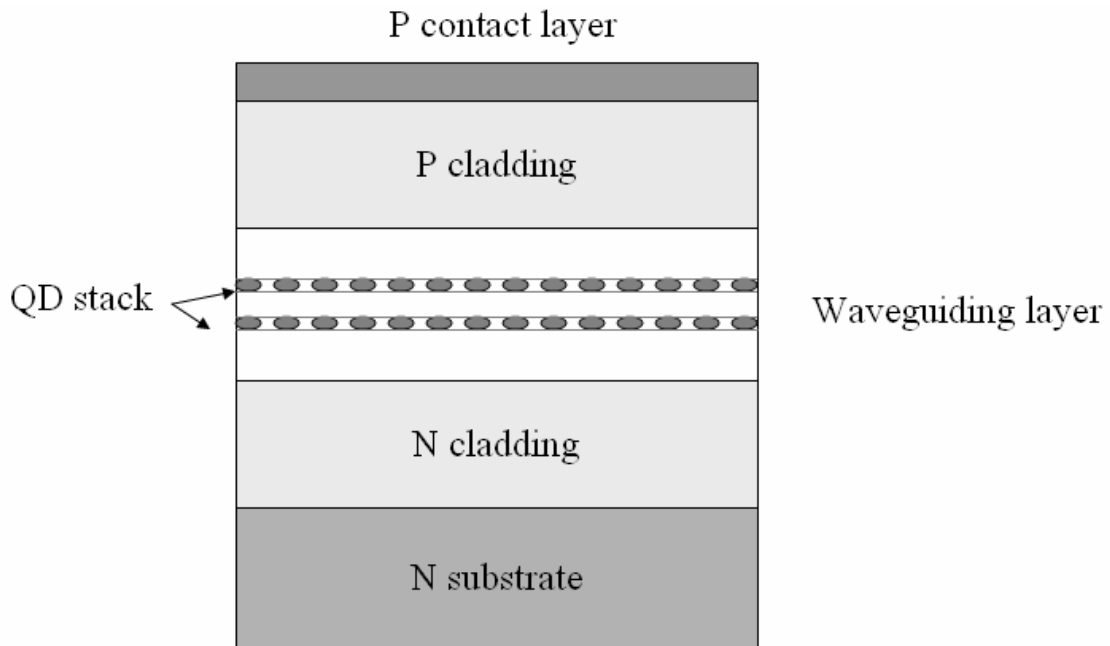


Figure 4.5 Epitaxial structure of a typical QD laser

The right choice of material is crucial because it affects the quality of dot formation and can cause significant amount of alloy and interface scattering if not chosen correctly. Also the cladding–waveguide interface should be band-engineered for efficient carrier injection into the active region. The appropriate combination of doping levels in each layer as shown in figure 4.5 is also of importance since it influences both cladding losses and device resistance.

Choice of waveguide:

The most common choice of waveguide material is 5% AlGaAs which has lower band discontinuity with the cladding AlGaAs layers compared to GaAs. Hence the forward voltage drop across the active region can be somewhat reduced. Also carrier confinement in the active region is stronger in 5% AlGaAs. Alternatively, GaAs waveguides have

already been demonstrated as a better candidate by keeping the losses at a very low level [8]. It is believed that growth of GaAs helps in planarizing growth surface fronts which results in less interface roughening and uniform crystal growth. Also it eliminates alloy fluctuations in waveguide which can cause additional scattering losses.

As for the cladding material choices, the choice of AlGaAs compounds are dictated by the quality of material grown in MBE system and the amount of modal overlaps in cladding region. The right decision can be made based on empirical results obtained from studying grown material quality. While in MOCVD lower Al content is shown to give better material growth, in case of MBE it is the other way around [52]. Therefore AlAs epilayers are of best quality having the least alloy scattering and furthermore the hole mobility is also higher in AlAs compared to 70% or 85% AlGaAs. Besides, AlAs has the smallest cladding overlap hence cladding losses can be minimized too. However in edge emitting lasers as the facets are exposed to air unlike VCSELs, AlAs decomposes even at room temperature causing mirror damage.

The other choice can be either 85% AlGaAs or 70% AlGaAs, both of which are widely accepted as cladding materials. In terms of heterobarrier discontinuity, 70% AlGaAs clearly has advantages but intuitively, 70% AlGaAs may give higher cladding losses than 85% AlGaAs. However, we have calculated the losses and comparison of the losses show that it does not differ too much. On the other hand local alloy fluctuation is smaller in 85% AlGaAs. So as mentioned earlier, either of the material can be suitable depending on the maturity of crystal growth which in turn depends on specific growth systems in use.

The other matter to consider is the doping profiles in the cladding to keep the cladding losses at the lowest level. The doping profile can be graded so that near the heterointerfaces the doping is lesser and as the mode tail drops, the doping level can be gradually increased. This scheme is advantageous since it doesn't increase the device series resistance too much which is the case in lightly doped cladding layers.

4.1.3 Device Features:

Processing is an integral part of implementing semiconductor devices on wafers having epitaxially grown active layers. The device pattern and geometry are defined by sequences of processing steps. Processing of the devices under consideration is quite straightforward since they are processed as simple edge-emitting waveguide structures using well-established and matured III-V GaAs/AlGaAs processing technology.

However there are specific aspects of processing that need to be carefully considered for high power lasers. The devices should be capable of handling high current density with improved heat management scheme. Additionally, the current needs to be effectively confined within the ridges; but more importantly since the sheet resistance scales down with the device area, it is more beneficial to have broader stripes. The decision of device size is therefore a compromise between these two issues. Narrower ridge widths ensure good confinement of current, on the other hand broader area stripes can sustain higher power. Narrow ridges also help reducing threshold current which leads to less heat dissipation but at the cost of higher waveguide losses. Typically ridge widths of 60 - 100 micron are chosen for high power diode lasers which perform reasonably well at high pumping level. In case of broad area devices, the device width is determined by the metal stripe width instead of the ridge width since there is negligible current spreading in lateral direction compared to the higher conduction path through the junction in transverse direction once the diode turns on. But it is very important to make sure that the adjacent ridges are electrically insulated from each other. Usually this is done by shallow mesa wet etching. This technique is particularly attractive because of its simplicity and also as no additional insulating layer is required (for example oxide layers), the thermal conductivity is not compromised either. The choice of metal is also crucial for high power operation because one of the most common reasons for device failure is contact burn out. We shall discuss the choice of p and n contact metals in experiment section.

Another essential feature dimension of the devices is their cavity length which is simply determined by cleaving the sample along $\langle 110 \rangle$ plane. The cleaved facets provide only 30% reflectivity which is inadequate for output coupling. Hence additional dielectric

mirror pairs are needed to be deposited on the facets. The mirror pairs normally used are MgF_2/ZnSe which gives reflectivity close to 98% when five pairs are used. This combination is also reliable on GaAs substrate having good surface adhesion and thermal match.

Once the device is processed, it has to be modified for mounting on systems suitable for high power calibration. The detailed processing sequence will be elaborated in following section 4.2.

4.1.4 Bonding, packaging and heat management issues:

When dealing with high current densities, mounting of devices can be a sensitive issue. In general, the cleaved devices are mounted epilayer up on a heat sink, which is typically a polished block of Copper. Electrically conductive silver epoxy can be used to bond the laser bars down to the Cu block. However there is a thermal mismatch between GaAs and Cu which can cause additional stress. Careful choice of solder materials such as Indium can relieve this stress. Also there should be good contact between the probe and the metal to keep the contact resistance very low. Specially designed gold tip probes are well-suited for high power characterization.

Epilayer up configuration has its advantages for example the as-cleaved mirror facets near the active region are left intact and pristine in this way. But the devices have to be polished and thinned down for efficient heat removal which makes them fragile to handle. So, in high power regime where there is substantial heat generated in the active region, it is better to mount the device epise down. This configuration can significantly improve device performance in CW condition [53].

Our initial devices that are presented here were run under pulsed condition hence there wasn't the urgency of heat removal. However once they operate in CW condition, custom designed conductively cooled packages with TE coolers can be used for better thermal management.

4.2 Experiments and Results

Here we describe the sequences of processing steps of the MBE grown sample to fabricate edge emitting lasers with a brief account of the growth conditions. Several devices were grown and processed in order to study the lasing condition in the quantum dot lasers. The characterization techniques are also outlined and finally selected device data obtained from the experiments are presented.

4.2.1 Device Fabrication and processing: The QD lasers were grown on epi-ready n^+ doped GaAs ((100) substrate in Applied Epi Gen III MBE system. The growth temperature for AlGAs cladding and waveguides were maintained at 590°C . During growth of QDs, the temperature was lowered down to 510°C . Description of the dots that are grown is given in chapter 2. The bottom cladding was Si doped at $2 \times 10^{18}\text{ cm}^{-3}$ and near the undoped waveguide, the doping was reduced to half. The top p cladding was doped with Be having similar doping profiles and finally the device was completed with a heavily doped contact layer reaching doping level around 10^{19} cm^{-3} . The cladding layer thicknesses were approximately 2 micron each and the waveguides were around 2200 \AA . In case of multistack QDs, the QD layers were separated by 300 \AA GaAs spacer.

The grown wafer is processed into broad area ridge waveguides having n and p ohmic contacts for electro-injection. The choice of metal is governed by the metal work function and the electron affinity of the doped semiconductor [54]. First of all, a piece is cleaved with minimum surface defect density. After thoroughly cleaning with Acetone, Isopropyl alcohol and DI water, the sample is dipped into aqueous HCl solution in order to remove any native oxide before metallization. The next step is metallization of n-contacts on the back side of the n^+ substrate. The n metal is usually deposited on the entire back surface for uniform injection of carriers and stable contact with the mount.

The n metal is comprised of Gold-Germanium alloy (AuGe , 400 \AA) followed by Nickel (Ni , 100°) and finally Gold (Au , 1000 \AA) that are sequentially deposited in UHV e-beam evaporator chamber. The AuGe forms alloy with GaAs while Ni acts as a diffusion barrier. Au is used as the top contact for its better electrical conductivity and stability

against oxidation. Once the n metal is formed, it is annealed in Rapid Thermal Annealing (RTA) furnace at 450°C for 30 sec which is purged with dry nitrogen during the process. The Ge atoms from Au-Ge diffuse into n+ GaAs to form low-resistance ohmic contact as the furnace temperature is well above the eutectic temperature (360°C). RTA also provides better adhesion to the surface [55].

The broad area ridges (typically 30-60 micron wide) are defined by the p metal stripes which are patterned using optical UV photolithography. Positive photoresist is used for higher resolution. After pattern registration, the sample is put back into the e-beam evaporator for p –metal deposition. The metal combination used as p contact is Chromium ($\text{Cr}, 350\text{\AA}$)/ Silver ($\text{Ag}, 2000\text{\AA}$) /Au(1000\AA). Here insertion of thick silver layer promotes better thermal conductivity and stability which is important for high drive current. The thick p metal also gives less voltage drop in in-plane direction [30]. This is then followed by a standard lift-off procedure upon immersing the sample in acetone. Finally to electrically isolate the ridges, isotropic wet etching is performed using H_2SO_4 : H_2O_2 : H_2O : : 1:8:80 . This etchant gives around 80\AA - 120\AA /sec etch rate on GaAs and AlGaAs at room temperature. Stripes of a 60-100 micron width are patterned to cover the metal ridges prior to etching. The feature sizes of the mesa are determined by the metal stripe width considering the consequences of lateral undercut of 2-3 micron on both sides. A small piece is first etched to calibrate for precision. Next the top contact layer and the p cladding are removed and the etch front stops at the undoped waveguiding region. Care should be taken not to etch down past the active region which can cause non-radiative recombination at the exposed side-walls. The last step is to cleave the processed sample into desirable lengths and mount them on Cu mounts using silver epoxy for characterization as described in previous section. The processed ridge waveguides are shown in the schematic below.

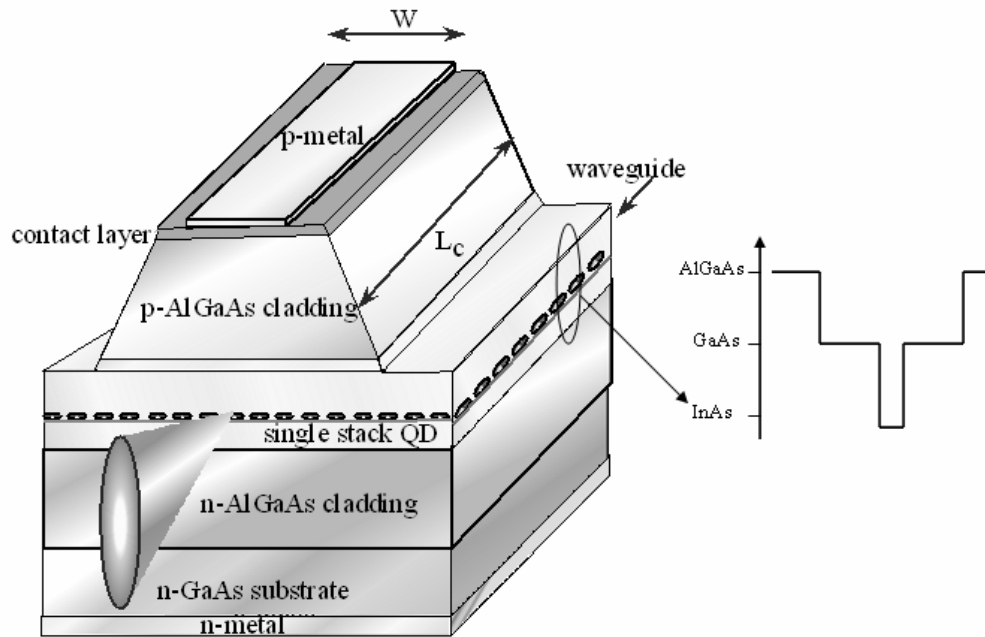


Figure 4.6 Processed QD broad area edge emitting laser used in the experiment

4.2.2 *Characterization of processed devices:* The characterization methods described here are Current-Voltage (I-V), Light –Current (L-I) and Electroluminescence (EL) , all of which were taken at room temperature. These techniques are fairly straightforward hence can be carried out routinely to provide rapid feedback for device design and crystal growth.

Once the devices are mounted, individual ridges are inspected to see if there is any current leakage or shorting of devices due to improper mounting. This is done by I-V characterization using curve tracer. I-V characterization is also particularly useful because it shows the device turn on which can reveal whether the p-n junction has any defects during growth. Typically for InAs QD lasers, the forward turn on voltage is 0.75 Volts.

The L-I experiments generate the threshold current and slope efficiencies of the lasers. The devices under test were driven by electric pulses having pulse width of 200 nSec and

0.5% duty cycle. The emitted light from the end facet was collected into a broad area Germanium detector. The L-I set up was calibrated for maximum light output collection. Once the devices show lasing behavior, EL experiment is carried out on selected devices that exhibit stable behavior well above threshold. The light output is coupled to a fiber which is connected to the entrance slit of a spectrometer. A liquid Nitrogen cooled Ge detector is placed at the exit slit of the spectrometer. The devices are driven above threshold and lasing output is collected by the fiber and spectral output is recorded and plotted via data acquisition software. Besides, to obtain the inhomogeneous linewidth of the QD ensemble, some spectral data are also taken for spontaneous emission below threshold.

4.2.3 Experimental results:

Initial attempts have been made to combine the narrow linewidth InAs QD ensemble (22 meV) into the waveguide structure. The waveguide material in all cases was 5% AlGaAs. However due to imperfect material quality, AlGaAs in particular ,the QDs tend to interdiffuse and broaden when grown within a laser cavity. Here we present device data of three different QD lasers that show room temperature lasing at reasonably low threshold current density.

The first device (run # SF 48) has three quantum dot stacks to ensure that the lasers have sufficient ground state gain to lase. The cladding material was 70% AlGaAs. As we see in the plot , ground state lasing at $\lambda=1.25$ micron was achieved having the threshold current density of 87 Amps/cm² which is comparatively higher owing to multiple stacks. However the spontaneous linewidth was measured 28 meV which is quite a bit of improvement considering that typical values are 35-36 meV.

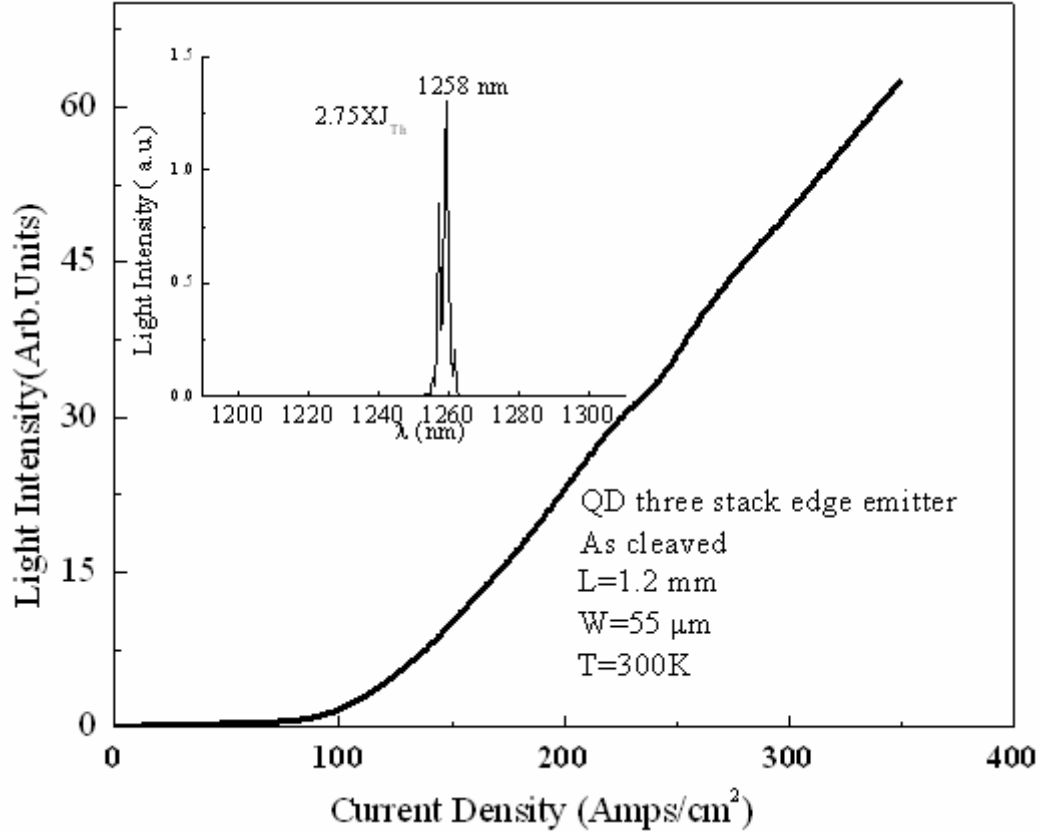


Figure 4.7 Lasing characteristics of triple stack QD laser at room temperature

The next device (run#53) had single stack quantum dots and the cladding material was 80% AlGaAs. Though the threshold current became less than half (43 Amps/cm²), however the spontaneous linewidth increased to 35 meV. The possible reason for broadening is attributed to increased surface roughness caused by 80% AlGaAs.

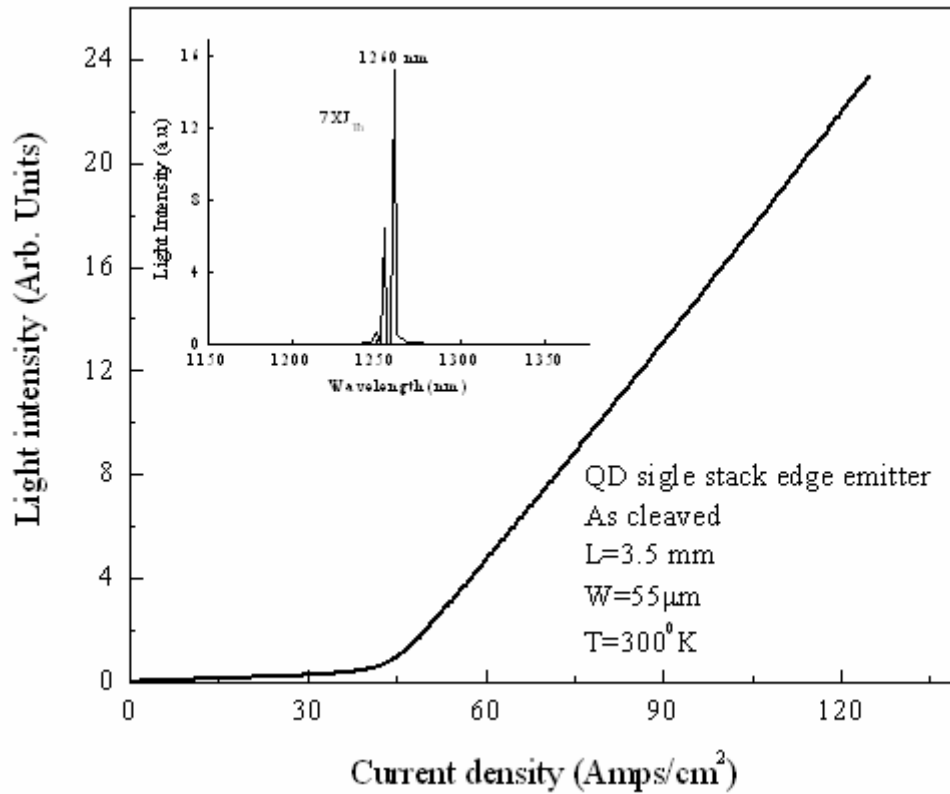


Figure 4.8 Lasing characteristics of triple stack QD laser at room temperature

To improve carrier confinement [49, 51], a different waveguide design with 70% AlGaAs and one micron thick 30% separate confinement heterostructure (SCH) was implemented (run# 74) but however both the threshold and the inhomogeneous broadening deteriorated. It is believed that the undoped SCH layer causes high voltage drop hence the threshold current increases which also shows poor thermal behavior. Moreover, 30% AlGaAs causes more surface roughening as well.

These device data reveal that dot uniformity is strongly correlated to the cladding material, mainly Aluminum composition. Besides it is critical to have the right

combination of waveguide/cladding material to suppress thermal escape of carriers which becomes more severe in high power domain. The threshold current data values give good insight into this issue. Therefore these laser data gives us sufficient feedback on how to improve and optimize the waveguide structure to obtain high quality quantum dots and ultimately achieve ultra low optical losses.

4.3 Summary: The critical design issues for realizing low internal loss and high efficiency QD laser diodes are addressed with especial emphasis on material selection for waveguide and cladding. The drawbacks associated with broadened waveguides and techniques to overcome those are proposed. The fabrication aspects to obtain the right kind of device features and dimensions for high power lasers are mentioned as well. In order to have reliable CW operation, the high power laser diodes should be capable of managing generated heat that has been outlined too.

A detailed account of fabrication and processing steps followed in implementing several QD laser diodes are given. Preliminary device data reveals valuable information regarding QD ensemble. It is believed that the quality of dots is seriously affected by the Aluminum composition of the underlying epilayers.

Chapter 5

Limitations of Planar Quantum Well Cascade Laser in High Operating Power Range

5.1 Introduction:

Quantum Cascade laser based on intersubband transition in Quantum wells has already been proven as a viable candidate for high power mid infra-red applications owing to its large gain due to multiple stages, non-existent Auger recombination and its wide tunability (3~ 160 μm) [14,56,57]. Achieving high continuous power at room temperature with high wall plug efficiency is a key requirement in order to develop compact systems having practical applicability. In spite of remarkable and steady advancement of basic design and material growth since its first demonstration over a decade ago, the planar QCL still suffers from low operating efficiency compared to diode lasers that severely restricts its performance at high level of continuous drive current. Often attributed to loss in injection efficiency [55,58,59], we alternatively propose that this inefficiency stems from a more fundamental limitation tied to the band structure of quantum wells themselves. The objective of this chapter therefore is to understand the physics of this basic limitation occurring in planar quantum well cascade lasers by investigating the limiting factors and their influence in power output. By doing so, we also evaluate the prospects of tailoring the basic parameters for substantially improving device performance.

The chapter is divided as follows: The key features of the QCL are discussed in section 5.2. In section 5.3 theoretical background is laid for understanding various scattering mechanisms of electrons occurring in QWs in a cascaded structure. Basic laser rate equations for QWCLs are derived in section 5.4 followed by presenting simulated results in 5.5. We also provide simulations based on realistic parameters that can be obtained in a QD cascade structure.

5.2 Basics of Quantum Cascade Laser:

The working principle of Quantum cascade laser is based on two specific schemes: Firstly, “*Unipolar Injection*” which implies intersubband or intersublevel optical transition within the conduction band as opposed to bipolar devices where the transition occurs between the conduction and valence band [60]. So the emission wavelength in QCL is totally free from band gap slavery and can be tuned over a wide range of wavelengths.

Secondly, “*Photon Recycling*”, which accounts for the cascading nature of carriers with multiple gain stages. These two unique criteria are shown in fig 5.1.

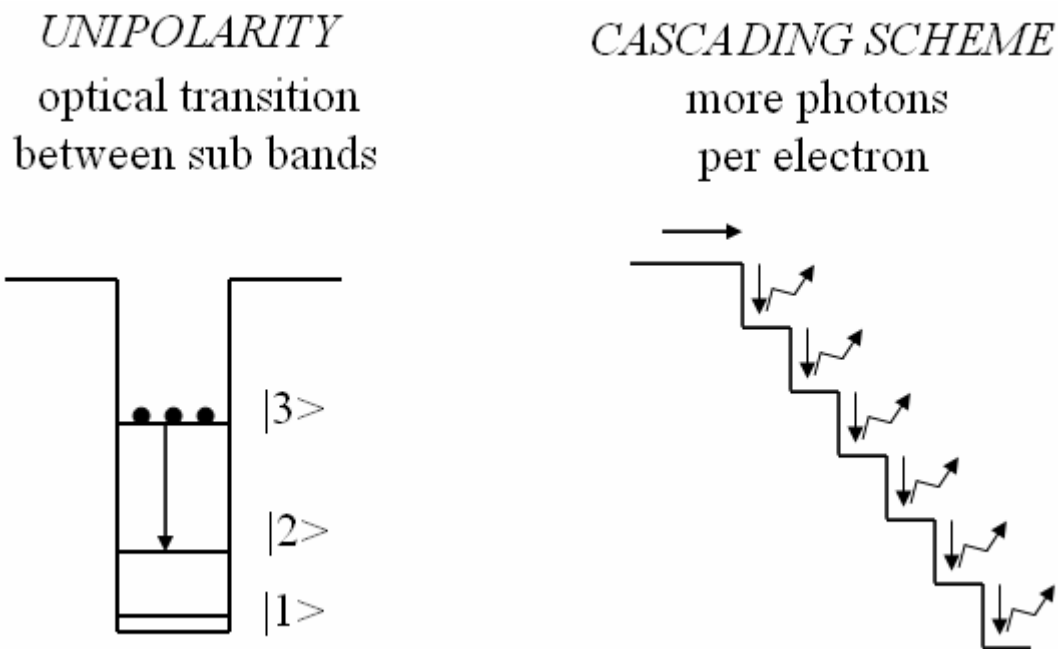


Figure 5. 1 Unipolarity and Cascading in QCL [60].

The QCL structure consists of multiple periods of cascaded injector-active region. Electron streams down energy staircase sequentially and every time it hits the step, it makes a quantum jump between well-defined energy levels emitting photon. A typical QCL structure having super lattice injector region and three coupled quantum well active region is illustrated in figure 5.2 [61,62].

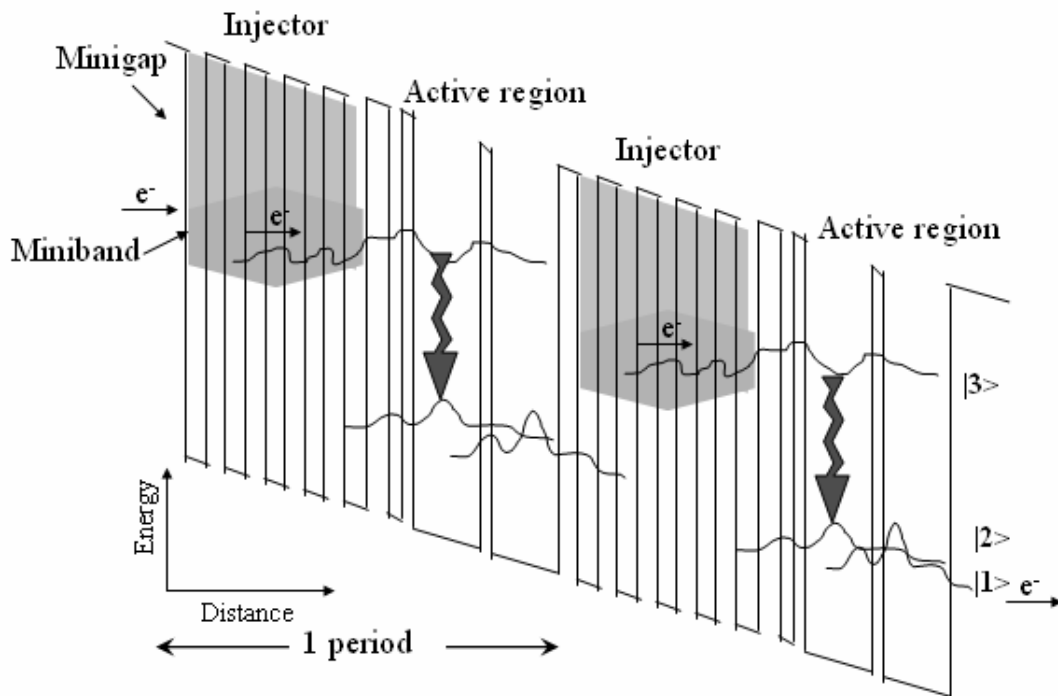


Figure 5.2 Basic operation of QCL [63]

Under appropriate bias condition, the conduction band acquires a stair case shape. The electrons are injected into the active region from the injector superlattice through a comparatively thick barrier. The structure is designed so that radiative transition occurs from $|3\rangle$ to $|2\rangle$ due to large oscillator strength. After making radiative relaxation, electrons escape from the active region to the next injector through another thick barrier. The mini band of precedent injector coincides with energy level E_3 in active region whereas the ground energy level E_1 is aligned with level E_3 of the following period to facilitate carrier injection into the active region. On the other hand, the injector mini gap blocks the electrons in $|3\rangle$ from tunneling into unwanted higher energy levels and escaping out of the active region. Carriers in level $|2\rangle$ are depopulated by relaxing down to $|1\rangle$ via optical phonon emission followed by tunneling into the next injector. In order to ensure population inversion in $|3\rangle$, the nonradiative scattering lifetime τ_{32} has to be longer than the lifetime τ_{21} . $|2\rangle$ is separated by an optical phonon energy (~ 30 meV) from $|1\rangle$ which strongly enhances the scattering of electrons out of state $|2\rangle$. Besides, the tunneling time out of $|1\rangle$ is also very fast, leading to rapid depopulation.

5.3 Intrsubband Scattering and Absorption Mechanism in QWCL

The understanding of electron relaxation mechanisms mainly scattering occurring within the conduction subbands is essential since they will be extensively used to model the QCL rate equations. In case of intersubband transitions, due to similar radius of curvature, the non-radiative scattering processes are due to electron-electron, electron - phonon and interface roughness scattering. In III-V semiconductors, by and large the dominant electron relaxation mechanism is scattering by Longitudinal Optical (LO) phonon which is governed by Fermi's golden rule [55,61,64,65].

The LO scattering can take place within the same subband in a QW as well since this process is always allowed as long as the energy jump is equal or greater than the LO phonon energy. But on the other hand as pointed out in Chapter 1, this type of transition is prohibited in QDs due to phonon bottleneck. The active region in a QWCL laser can be treated as a three -level system with each level containing certain population of electrons

which scatter between the subbands by emitting LO phonon or photon [14,66]. These scattering mechanisms are elucidated in the band structure diagram below in figure 5.3. We have only included sublevels $|2\rangle$ and $|3\rangle$ here and omitted the lowest state $|1\rangle$ for the sake of simplicity since due to extremely fast tunneling time τ_1 there is hardly any build-up of carriers in $|1\rangle$, so the electron population is virtually zero. We also assume all the subbands are ideally parabolic with equal in plane effective masses. Besides, it is inferred that the electrons high up in energy in each subband i.e. the “hot” electrons thermalize rapidly to the bottom of the subband in the thermal pool. So they are in quasiequilibrium condition and can be described by respective Fermi functions.

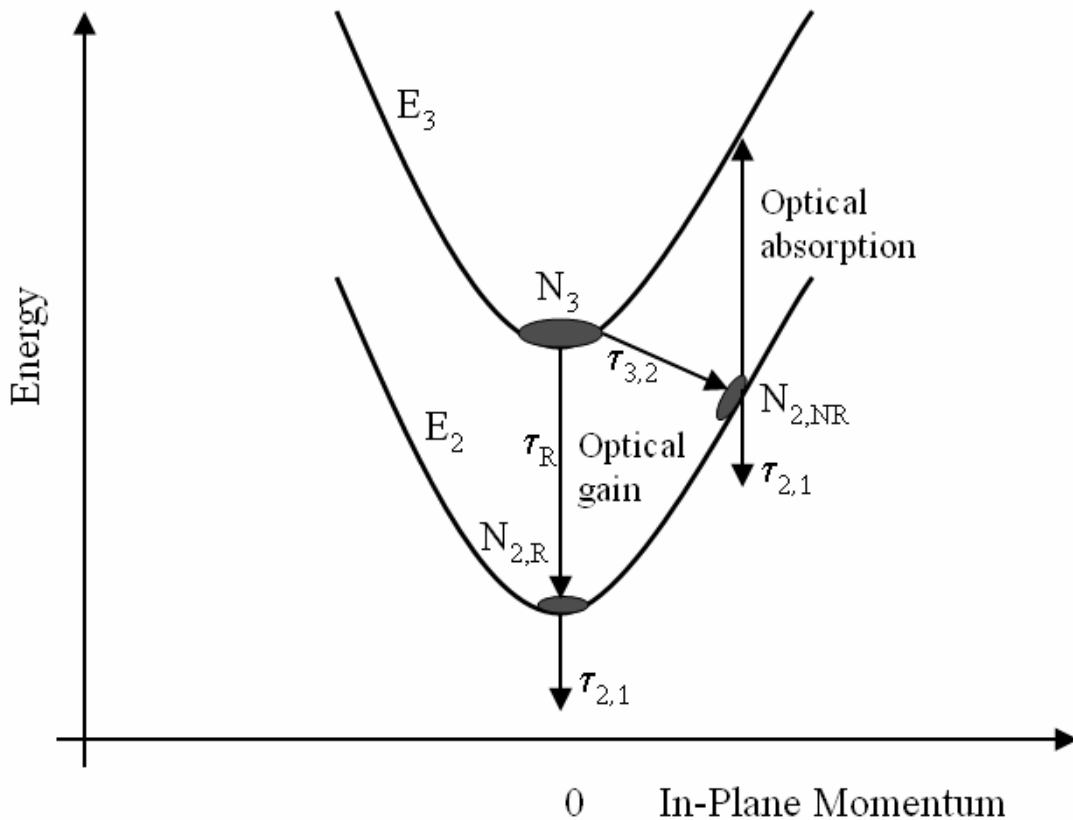


Figure 5.3 Scattering routes in subband $|3\rangle$ and $|2\rangle$ showing internal absorption

Referring to the figure, N_3 is the steady state population in sublevel $|3\rangle$ which is determined by the pump level. The electrons in $|3\rangle$ make radiative transition down to $|2\rangle$ emitting a Mid-IR photon at a spontaneous rate of τ_R^{-1} contributing to population $N_{2,R}$. This emission rate can be expressed by the same equation (3.19) used for electron-hole laser in chapter 3 with appropriate dipole strength and frequency. The other channel from $|3\rangle$ to $|2\rangle$ is through nonradiative transition where an electron emits an LO phonon. This relaxation involves large in-plane momentum transfer with a characteristic scattering lifetime of τ_{32} . As depicted in figure, this results in population $N_{2,NR}$ in $|2\rangle$ which is at a different E-k position than $N_{2,R}$. Carriers within both $N_{2,R}$ and $N_{2,NR}$ relax down to $|1\rangle$ by zero momentum transfer at a very fast rate of $\tau_{2,1}$ and escape to the next gain stage. However, $N_{2,NR}$ reabsorb photon and make vertical absorption transition up to $|3\rangle$ again. The electrons moving upward in this way join the hot electrons in $|3\rangle$ and increase the electron temperature. Eventually they may thermalize down to the electron pool or escape to continuum. Comparing these two branches based on the typical time constants, for

example: $\tau_{3,2} \sim 1.2$ ps and $\tau_{2,1} \sim 0.5$ ps [67], this nonradiative population, $N_{2,NR} \approx \frac{\tau_{2,1}}{\tau_{3,2}} N_3$

consumes approximately 40% of the gain population. For ideally parabolic bands, this vertical reabsorption transition of an electron from population $N_{2,NR}$ exactly matches the gain in a vertical radiative transition from $|3\rangle$ to $|2\rangle$. With nonparabolicity, this absorption can be bigger or smaller depending on the details related to the density of the final states at the upper energy transition. Unlike free carrier absorption losses, this loss mechanism that we define as $\alpha_{N_{2,NR}}$ is significantly stronger than free carrier absorption since it directly absorbs photon. The total internal loss then becomes: $\alpha_i = \alpha_{\text{free carrier}} + \alpha_{\text{scattering}} + \alpha_{N_{2,NR}}$. This internal absorption mechanism is inherent to planar QWCL due to their upward E-k curvatures of gain level $|3\rangle$ and $|2\rangle$. The same process does not occur in electron-hole lasers because of the opposite curvature of the E-k dependence of the conduction and valence bands in a planar quantum well. This absorption loss is significant at low temperature as well. Moreover, it depends on cavity length through the dependence of N_3 hence gives an artificial appearance of low injection efficiency η_i . This

additional internal absorption therefore represents a fundamental limitation to maximum attainable efficiency in QCL and apparently can not be eliminated.

5.4 Rate equation analysis:

Here laser rate equations pertaining to subband $|3\rangle$ and $|2\rangle$ are analyzed to describe the operating characteristics of a QWCL based on real device data that have demonstrated significant results in CW mode [68,69,70]. The steady state solution to the rate equations are used to illustrate carrier scattering between $|3\rangle$ and $|2\rangle$.

The influence of internal absorption is analyzed by including the internal absorption due to the population $N_{2,NR}$. The rate equation for the photon number is then given by

$$\frac{dn}{dt} = -\frac{\omega_c}{Q}n + G_o(N_3 - N_{2,R})(n+1) - G_oN_{2,NR}n \dots\dots\dots (5.1)$$

where n is the photon number, G_o is the gain coefficient and cavity loss rate $\frac{\omega_c}{Q} = \frac{v_g}{L} \ln\left(\frac{1}{R_B R_F}\right) + \alpha_{FC}$. Here ω_c is the lasing frequency, Q is the quality factor α_{FC} is the free carrier absorption, v_g is the group velocity of the wave along the waveguide, L is the cavity length, R_F and R_B are front and back mirror reflectivities respectively. The free carrier absorption is due to both the built-in electron concentrations in the doped regions and electron concentration in the active region.

The electron populations in the three relevant E-k positions are given by

$$\frac{dN_3}{dt} = N_G \frac{JWL}{q} - G_o(N_3 - N_{2,R})(n+1) - \frac{n_{th}+1}{\tau_{3,2}}(N_3 - N_{2,NR}) \dots\dots\dots (5.2)$$

$$\frac{dN_{2,R}}{dt} = G_o(N_3 - N_{2,R})(n+1) - \frac{n_{th}+1}{\tau_{2,1}}N_{2,R} \dots\dots\dots (5.3)$$

and

$$\frac{dN_{2,NR}}{dt} = \frac{n_{th}+1}{\tau_{3,2}}(N_3 - N_{2,NR}) - G_oN_{2,NR}n - \frac{n_{th}+1}{\tau_{2,1}}N_{2,NR} \dots\dots\dots (5.4)$$

In equations (5.2) through (5.4) N_G is the number of gain stages, J is the injection current density, W is the stripe width, and n_{th} is the thermal phonon number in an optical phonon mode given by Bose-Einstein factor as follows:

$$n_{th} = \frac{1}{\exp(\hbar\omega_{LO} / kT) - 1} \dots\dots\dots(5.5)$$

At room temperature, $n_{th} \approx 0.4$. We assume that $\tau_{3,2}$ and $\tau_{2,1}$ are due to optical phonons with different momentum.

To evaluate the impact on the QCL operation, the rate equations (5.1) through (5.4) are solved at steady state in a self consistent manner including optical losses and carrier population in each subband. Based on the solution, the power output as a function of injection current can be calculated. The output optical power extracted from single facet in terms of photon density $n(J)$ is then given as:

$$P_0(J) = \frac{v_g}{2L} \hbar\omega_c n(J) \ln \frac{1}{R_F} \dots\dots\dots(5.6)$$

The wall plug efficiency expression is similar to the one derived for electron-hole laser in chapter 3 as shown:

$$\eta_{WP} = \eta_i \frac{\hbar\nu_{ph} / q}{J\rho_s + V_F} \frac{J - J_{th}}{J} \frac{\ln(1/R_F)}{\ln(1/R_F) + \ln(1/R_B) + 2\alpha_i L} = \eta_i \frac{\hbar\nu_{ph} / q}{J\rho_s + V_F} \frac{J - J_{th}}{J} \eta_{op} \dots\dots\dots(5.7)$$

With the only exception of including the absorption loss $\alpha_{N2,NR}$ in the internal loss term. Once the L-I responses are calculated, optical efficiency is extracted from the slope efficiency of the L-I curves.

Founded on these solutions, following section presents simulations showing the impact of internal absorption term and time constant τ_{32} in efficiency characteristics of a QWCL.

5.5 Calculated results and discussion

The CW high power operating characteristics of QCL are evaluated by examining the simulated light vs. current plots based on parameters of QCLs exhibiting superior room temperature high power performance to the best of our knowledge. The device structure parameters such as modal confinement, waveguide losses etc are calculated based on a real QCL and the device features and dimensions are typical of QCLs that have demonstrated room temperature CW operation [68,69,70,71]. The numerical calculations are generated for room temperature condition and the LO phonon energy used here is 34 meV.

In particular the contribution of internal absorption to determining the injection efficiency η_i is investigated. Moreover it is also shown how threshold and optical efficiency are influenced by time constant τ_{32} and results are computed based on longer time constant showing significant improvement in internal absorption and optical efficiency.

5.5.1 Impact of Internal Absorption on injection efficiency:

Figure 5.4 shows the Light vs Current plots for a particular QCL design having $\tau_{3,2} = 1.25$ ps, $\tau_{2,1} = 0.5$ ps, $N_G = 30$, stripe width of 11 μm , cavity lengths of 2, 4, or 6 mm and reflectivities of $R_B = 0.95$ and $R_F = 0.29$. Gain coefficient is estimated to be $G_o L = 3,400$ cm/s which is selected on the basis of reported threshold current and relaxation τ_{32} [71]. Internal loss due to scattering and free carrier absorption in the doped regions is taken as $\alpha_{sc} + \alpha_{FC,doped} = 2$ cm⁻¹, while the free carrier loss $\alpha_{FC,active}$ due to the gain stages is calculated from the actual populations N_3 , $N_{2,NR}$, and $N_{2,R}$ and is included but $\alpha_{FC,active} \leq 0.1$ cm⁻¹. Other parameters are discussed below.

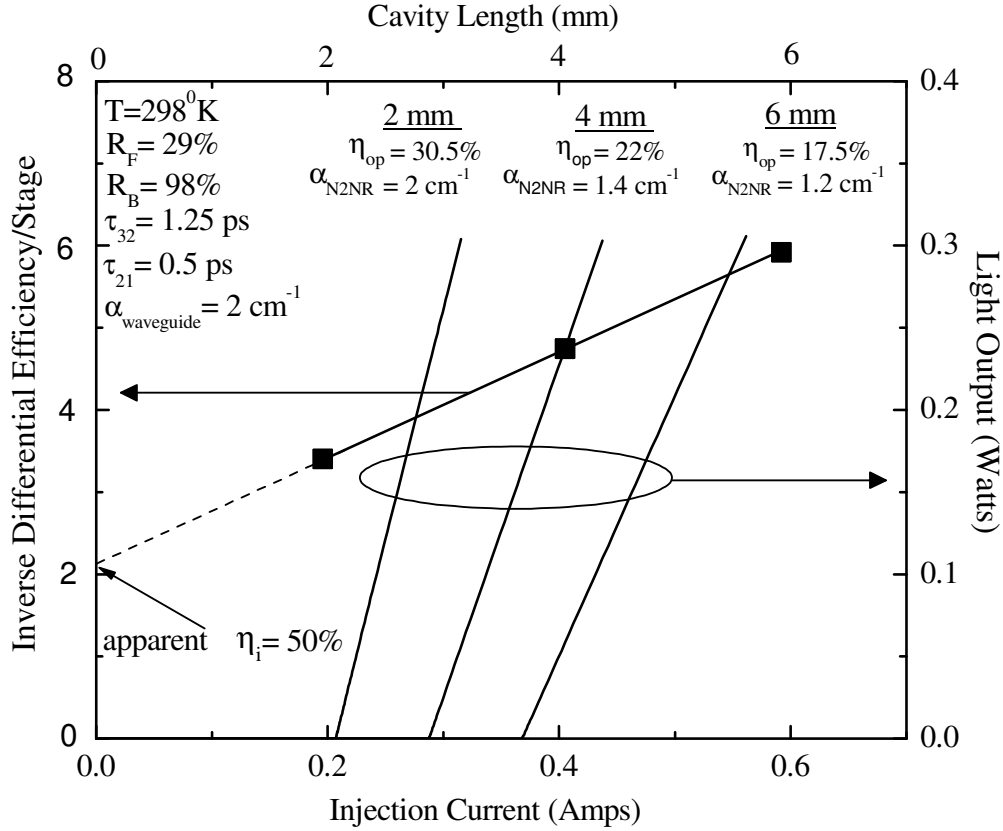


Figure 5.4 Calculated L-I plots of planar QCL for 2 m , 4mm and 6 mm cavity lengths. The injection efficiency is extracted from the inverse differential efficiency values using data points denoted by black squares.

The rate equations in (5.1) through (5.4) assume that the internal injection efficiency for each gain stage is $\eta_i = 100\%$ (3000% for 30 gain stages). The optical extraction efficiencies η_{op} are due only to internal optical losses and output coupling and are found from the calculated slope efficiencies of Fig. 5.4 for each cavity length to be $\eta_{op} = 31\%$ for $L = 2\text{ mm}$, $\eta_{op} = 22\%$ for $L = 4\text{ mm}$, and $\eta_{op} = 17\%$ for $L = 6\text{ mm}$. It is worth noting that the wall-plug efficiency will never exceed η_{op} , as it is the product of the efficiencies in equation (5.7). The dominant loss is due to internal absorption by $N_{2,NR}$, and these absorption values for each cavity length are given in Fig. 5.4 as 2.0 cm^{-1}

, 1.4 cm^{-1} and 1.2 cm^{-1} for $L = 2, 4$ and 6 mm respectively. Despite that the equations set the internal injection efficiency per gain stage to 100%, the standard approach of plotting the inverse slope efficiency vs. cavity length to find the $L = 0$ intercept produces an apparent injection efficiency of only $\eta_i = 50 \%$ per gain stage [72,73]. The apparently low η_i is produced erroneously because of the cavity length dependence of the internal absorption $\alpha_{N,2NR}$. This can lead to confusion over the separate contributions from internal loss and injection efficiency in limiting wall-plug efficiency. In fact, the experimental slope efficiencies of QCLs are low even for low operating temperature for which the injection efficiency η_i should be close to 100%.

As discussed in previous chapters, for electron-hole lasers achieving high wall-plug efficiency has required minimizing the internal loss to increase the cavity length and minimize electrical resistance, along with a high output coupling mirror (low reflectivity). In addition, the threshold current density must be minimized so that it has little contribution at the desired operating current density to give high $(J - J_{th})/J$. However, the absorption that results from phonon emission in the planar gain stage limits the effectiveness of using a long cavity combined with high output coupling, since high output coupling increases the threshold gain and simultaneously the internal loss.

To verify this we calculated light vs. current density curves for the same device parameters as above but with an output coupling reflectivity of $R_F = 0.05$ as in Fig. 5.5 for $\tau_{3,2} = 1.25 \text{ ps}$. In this case, decreasing R_F makes only a slight improvement in the operating characteristics because of the increased internal absorption. The $\alpha_{N,2NR}$ values now become 3.8 cm^{-1} , 2.3 cm^{-1} and 1.8 cm^{-1} for $L = 2 \text{ mm}$, 4 mm and 6 mm respectively with threshold current densities nearly twice as much as before.

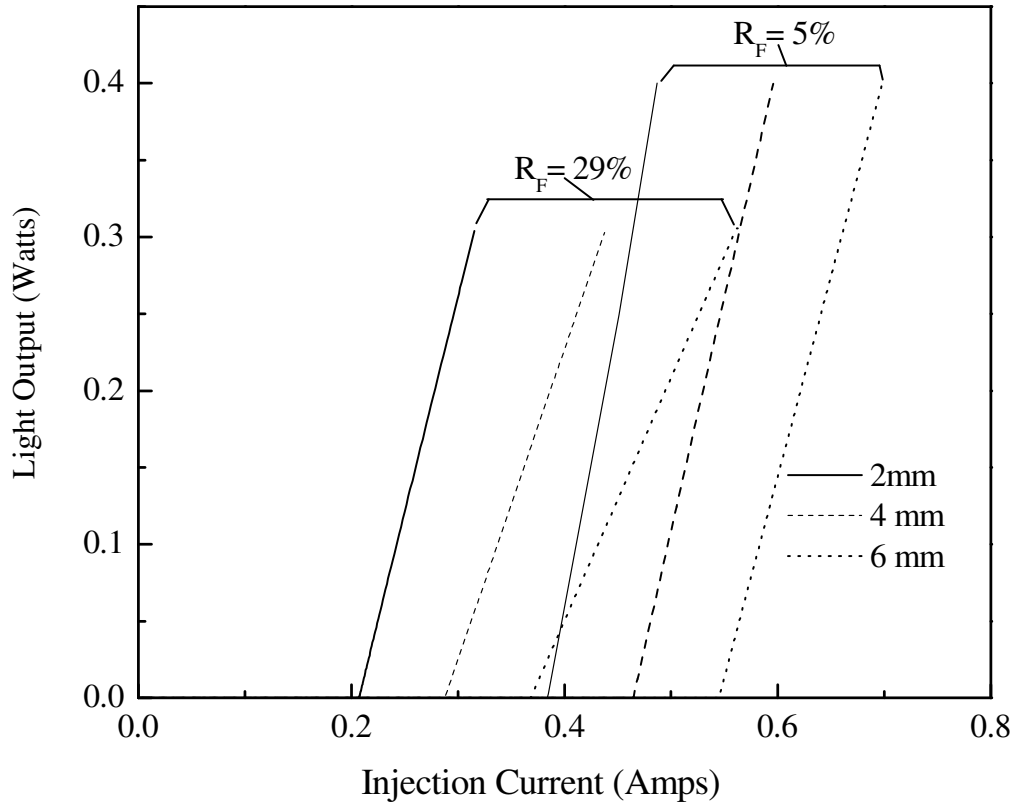


Figure 5.5 Same L-I plots calculated for 5% Reflectivity .The 29% reflectivity values are shown for comparison.

5.5.2 Projected results for QDs with longer τ_{32} :

As mentioned in Chapter 1, owing to discrete energy spectrum, the optical phonon scattering is greatly suppressed in a QD in the presence of “phonon bottleneck”. The phonon mediated relaxation time τ_{32} can therefore be substantially longer in a QD [74]. On the contrary, the phonon emission rates of a planar gain stage QCL have already been optimized using the three level approach to provide a fast relaxation path from level 2 through resonant optical phonon emission. So as long as the gain stage is planar, it may not be possible to increase τ_{32} .

Here we calculate L-I characteristic employing same device data but with longer τ_{32} having values of 5 ps and 25 ps in order to investigate effect of slow relaxation in device performance.

Figure 5.6 shows L-I plots for similar device parameter as fig 5.5. with two more sets of LI having longer τ_{32} . The results shows that even a moderate increase in τ_{32} has a dramatic impact on not only the threshold current, as expected, but also on the optical extraction efficiency because of the decrease in internal absorption.

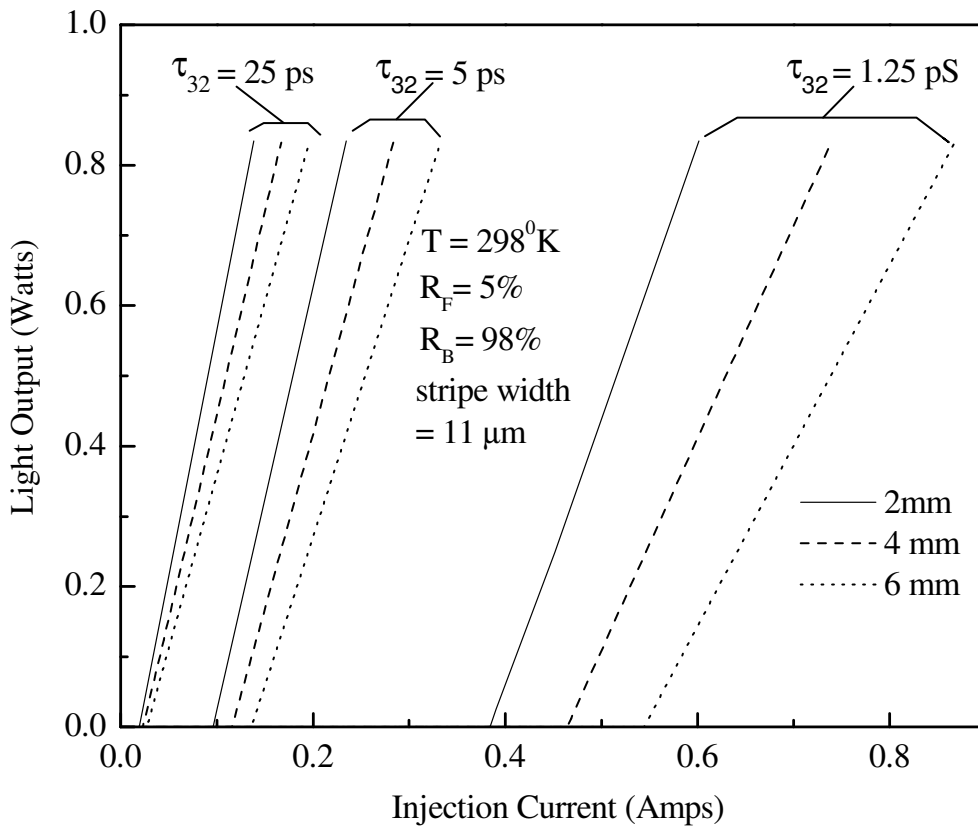


Figure 5.6 Simulated L-I plots showing huge improvement of slope efficiency and threshold for longer relaxation time

The effect on internal absorption is shown in Fig. 5.7. When $\tau_{3,2} = 1.25$ ps as typical for planar gain stage QCLs, $\alpha_{N_{2,NR}}$ can make up more than 50% of the total internal absorption above threshold. The dashed and solid curves in Fig. 5.7 for $\tau_{3,2} = 1.25$ ps show that decreasing the output mirror reflectivity simply increases the internal absorption, in our case from $\alpha_{N_{2,NR}} \approx 1.5 \text{ cm}^{-1}$ to $\alpha_{N_{2,NR}} \approx 2.5 \text{ cm}^{-1}$ for the 4 mm cavity length. As shown for $\tau_{3,2} = 5$ ps or $\tau_{3,2} = 25$ ps, even a slight increase in $\tau_{3,2}$ decreases this internal absorption by increasing the ratio $\tau_{3,2}/\tau_{2,1}$, which decreases $N_{2,NR}$. These results unambiguously demonstrate that simply by making $\tau_{3,2}$ even a few times longer can bring dramatic improvement in device performance.

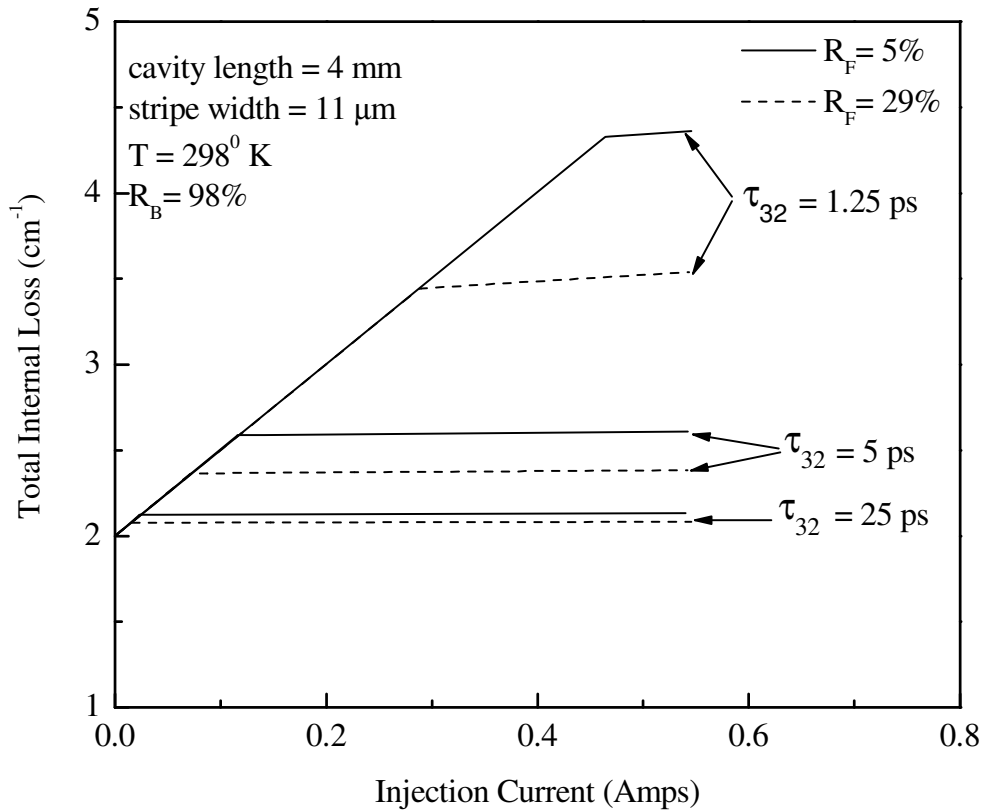


Figure 5.7 Effect of longer relaxation time on reducing internal absorption loss

There is yet another added benefit of having longer $\tau_{3,2}$ in the gain stage. It can be readily explained that gain compression phenomena is more severe in QCL compared to electron-hole laser owing to fast relaxation mechanism that depletes the gain population rapidly. So it is clearly evident that introducing QDs in the gain stage will help avoid early gain compression hence lower down threshold and internal losses even more.

5.6 Conclusion:

In this chapter we have investigated the loss mechanisms occurring in a planar gain stage QCL. In sharp contrast to an electron-hole semiconductor laser, a QCL is shown to suffer a severe internal absorption problem that is intrinsic to its planar gain stage. The internal absorption is caused by phonon emission of electrons and represents a possible limitation to wall plug efficiency while giving an artificial appearance of low injection efficiency due to cavity length dependence. This severity can be compensated by introducing lateral confinement of electrons based on quantum dots which can bring further improvement through reduction in threshold and less temperature sensitivity. However some other limiting factors that can affect high power CW operation have not been considered here for example device heating issues which results in deterioration in injection efficiency and threshold current. But the QCL experimental results show low efficiency even at low temperature which validates the presence of internal absorption. Nonetheless, introducing additional degree of quantum confinement in the gain stage can substantially enhance high power operating characteristics of QCL in every possible way.

Chapter 6

Summary of Research and Future Direction

The research work presented in this dissertation reflects a comprehensive effort to analyze and optimize high power semiconductor laser performance through achieving ultra low optical losses in the gain material. Currently considerable internal losses in planar QW lasers which is inherent to the QW active region itself, is identified as the biggest challenge in achieving continuous high power with high wall plug efficiency. This implies the necessity of introducing a totally new approach to circumvent the high power limitation. Through quantum confinement in all directions, self assembled III-V QDs open up a unique opportunity to extend the high power operating regime to an unprecedented level. Very promising QD laser efficiency characteristics have already been reported by other groups showing significant improvement over QW counterpart [75].

In this research treatise, we provide a detail theoretical analysis of QD edge emitting lasers based on real experimental parameters and demonstrate that by combining these QDs in a suitable low loss cavity, internal optical losses as low as 0.05 cm^{-1} can be achieved which allows the laser cavity length to extend to centimeter ranges . This ensures high power collection from the lasers while maintaining reasonably high conversion efficiency. The QD laser calculation is based on harmonic oscillator model and the device parameters are solved in a self-consistent matter imposing quasi-equilibrium and charge –neutrality condition in the active region. Various low loss waveguide models were examined to explore the feasibility of employing QD ensembles in the laser cavity. With the help of our simulations and models, suitable design rules were developed in order to implement ultra low loss long cavity QD lasers.

One of the major problems in achieving truly ideal delta like density of states to harvest the benefits of QD is its inhomogeneous broadening. Therefore our initial stage of investigation was mostly directed towards introducing small linewidth QD ensemble having only 22 meV broadening in a waveguide. Our primary device data points to the

fact that numerous parameters are needed to be optimized to obtain high quality dot material, most importantly the cladding and waveguide material.

We have also extensively studied the high power operating characteristics of unipolar QCLs which are primarily different from electron-hole lasers. It is of our firm opinion that the high power performance of planar gain stage QCL is strongly influenced by internal absorption in the gain medium due to fast intersubband phonon relaxation . An in depth- analysis of rate equations and their solutions exhibit that this inherent loss mechanism appears as a reduction in injection efficiency through its cavity length dependence and this can be compensated by cutting down this relaxation branch. We propose that owing to discrete delta like density of states, the QDs are capable of greatly suppressing this electron-phonon interaction hence enabling high power high efficiency device applications in Mid and Far –IR ranges.

Future direction:

Extensive research attempt is underway in order to implement high power QD lasers that can enable highly reliable operation at high powers and over wide operating temperature with high efficiency. Several possibilities will be explored for example:

- Better understanding and improvement of crystal growth quality through using ultra-pure source material in a clean system hence keeping the scattering loss and background doping at a minimum
- Incorporation of graded super lattice type cladding layers to facilitate electron transport into the waveguiding region.
- Using miscut wafers for crystal growth for better dot density and uniformity etc.
- Employing lithographically defined all epitaxial structure for excellent current and mode confinement
- Introducing fiber grating stabilized long cavity lasers etc to name a few.

As a final conclusion, the concept of ultra low loss in QD gain material definitely proves advantage over already well-established planar QW lasers and is a potentially viable candidate to be developed towards commercial devices. As more is understood about the

fundamentally unique physics of the QDs together with the technological advancements, it can create newer frontiers of novel device application with revolutionary functionalities such as photonic crystal and nano device technologies.

References cited in this dissertation:

- [1] D. F. Welch, "A brief history of high-power semiconductor lasers," *IEEE J. of Selected Topics in Quantum Electron.* Vol.6, no. 6, pp. 1470-1477 (2000).
- [2] R. Williamson, and M. Kanskar, "Improving the efficiency of high-power diode lasers," *Compound Semiconductors* (July 2004).
- [3] P.M.Smowton, J.D. Thomson, M.Yin, S.V. Dewar, P. Blood, A.C. Bryce, J.H. Marsh, C.J. Hamilton, and C.C. Button, "Optical loss in large optical cavity 650 nm lasers," *Semicond. Sci. Technol.*, Vol. 16, pp. L72-L75 (2001).
- [4] *Opto & Laser Europe*, July 8, (2004).
- [5] G.P Agrawal and N.K Dutta, "Long-Wavelength Semiconductor Lasers," Van Nostrand Reinhold Company (1986).
- [6] N.A. Pikhtin, S.O. Slipchenko, Z.N. Sokolova, and I.S. Tarasov, "Internal Optical loss in semiconductor lasers," *Semiconductors*, Vol. 38, no. 3, pp.360-367 (2004).
- [7] Alfalight press release 11/10/2004
- [8] N.A. Pikhtin, S.O. Slipchenko, Z.N. Sokolova, A.I. Stankevich, D.A. Vinokurov, I.S. Tarasov, and Zh. I. Alferov, "16W continuous-wave output power from 100 μm -aperture laser with quantum well asymmetric heterostructure," *Electron. Lett.*, Vol. 40, no 22, pp. 5885-5886 (2004).

- [9] Y. Arakawa and H. Sakaki, "Multidimensional Quantum Well Lasers and Temperature Dependence of Its Threshold Current," *Appl. Phys. Lett.*, Vol.40, no.11 , pp. 939-941 (1982) .
- [10] Y. Arakawa and A. Yariv, "Quantum Well Lasers---Gain, Spectra , Dynamics (Invited Paper)," *IEEE J. Quantum Electron.* Vol. 22, pp.1887-1889 (1986).
- [11] Mashiro Asada, Yasuyuki Miyamoto, and Yasuharu Suematsu, "Gain and threshold of three-dimensional quantum -box lasers," *IEEE J. Quantum Electron.* Vol.22, no.9, pp. 1915-1921(1986)
- [12] D. G. Deppe, and H. Huang, " Quantum Dot lasers," *Advanced Semiconductor and Organic Nano-Techniques (Part I)*, H. Morkoc (Ed.), Copyright© 2003, Elsevier (USA).
- [13] L. V. Asryan, and R. A Suris, " Theory of Threshold Characteristics of Quantum Dot Lasers: Effect of Quantum Dot Parameter Dispersion," *International Journal of High Speed Electronics and Systems*, Vol. 12, no 1, pp. 111-176, 2002. © World Scientific Company.
- [14] F. Jerome, F. Capasso ,C. Sirtori , D. L. Sivco , A. L. Hutchinson, and A. Y. Cho, " Quantum Cascade Laser," *Science*, Vol. 264, pp. 553-556 (1994).
- [15] N. S. Wingreen, and C. A. Stafford, "Quantum-Dot Cascade Laser: Proposal for an Ultralow-Threshold Semiconductor Laser," *IEEE J. Quantum Electron.*,Vol. 33, no. 7, pp. 1170-1173 (1997).
- [16] C. Hsu, J. O, P. Zory, and D. Botez, "Intersubband Quantum-Box Semiconductor Lasers," *IEEE J. Select. Topic Quantum Electron*, Vol. 6, no. 3, pp. 491-503 (2000).

- [17] R. Dingle, and C. H. Henry” Quantum Effects in Heterostructures,: U.S Patent 3982207.
- [18] Y. Nagamune, S. Tsukamoto, M. Nishioka and Y. Arakawa, “Growth process and mechanism of nanometer-scale GaAs dot-structures using MOCVD selective growth ,”*J. of Crystal growth*, Vol. 126, no. 4, pp. 707-717 (1993).
- [19] H. Fujikura, T. Muranaka, and H. Hasegawa, “ Formation of device-oriented InGaAs coupled quantum structures by selective MBE growth on patterned InP substrates,” *Physica E.* , Vol. 7, pp.864-869 (2000).
- [20] I.N. Straski, and L. Krastanow, Akad. Wiss. Wien, Math,-Naturwiss. K1 I Ib 146, 797 (1939).
- [21] L. Goldstein, F. Glas, J.Y. Martin, M.N.Charasse , and G. Le Roux, “Growth by molecular beam epitaxy and characterization of InAs/GaAs strained –layer superlattices,” *Appl. Phys.Lett.*, Vol. 47, no. 10 , pp. 1099-1101 (1985).
- [22] N. N Ledenstov, V. M Ustinov, D Bimberg, J A. Lott, and Zh. I Alferov, “ Applications of Quantum Dots in Semiconductor Lasers,” *International Journal of High Speed Electronics and Systems*, Vol. 12, no. 1 pp. 177-205, 2002, ©World Scientific Publishing Company.
- [23] Werner Seifert, Jonas Johansson, Niclas Carlsson, Anders Gustafsson, Jan-Olle Malm, “Continuous and discontinuous metal-organic vapour phase epitaxy of coherent self-assembled islands:: effects on size homogeneity ,”*J. Cryst. Growth* ,197,no.1-2, pp. 19 -24(1999) .

- [24] Albert-Laszlo Barabasi, "Self-assembled island formation in heteroepitaxial growth," *Appl. Phys. Lett.*, Vol. 70, no. 19, pp.2565 -2567(1997) .
- [25] Y. Chen and J. Washburn, "Structural Transition in Large-Lattice-Mismatch Heteroepitaxy ," *Phys. Rev. Lett.* Vol.77, no.19, pp. 4046-4049 (1996).
- [26] R. Songmuang, S. Kiravittaya, O.G. Schmidt, "Shape evolution of InAs quantum dots during overgrowth," *J. Cryst. Growth*, Vol.249 ,no.3-4, pp. 416-421 (2002) .
- [27] O. B. Shchekin, "Charge control and energy level engineering in quantum dot laser active region", Ph.D. dissertation, (University of Texas at Austin, Austin, TX, 2003)
- [28] V.M. Ustinov, A. E. Zhukov, A.Y. Egorov, and N.A.Maleev, "Quantum Dot Lasers," Oxford University Press (2003).
- [29] O. B. Shchekin, "Development of GaAs based Quantum Dot Edge-Emitting laser Operating at the Wavelength of 1.3 μm ," M.S. Thesis, (University of Texas at Austin, Austin, TX, 1999).
- [30] G.Park, "GaAs-based long wavelength quantum dot lasers", Ph.D. dissertation, (University of Texas at Austin, Austin, TX, 2001).
- [31] D. G. Deppe, D. L. Huffaker, S. Csutak, Z. Zou, G. Park, and O.B. Shchekin, "Spontaneous emission and threshold characteristics of 1.3- μm InGaAs-GaAs quantum-dot GaAs-based lasers,"*IEEE J. Quant. Electron.* Vol.35, no. 8 ,pp.1238-1246 (1999) .

[32] Krishna, S.; Zhu, D.; Xu, J.; Linder, K.K.; Qasaimeh, O.; Bhattacharya, P. Huffaker, D.L., “Structural and luminescence characteristics of cycled submonolayer InAs/GaAs quantum dots with room-temperature emission at 1.3 μm ,” *J. Appl. Phys.* Vol.86,no.11 , pp.6135-6138 (1999) .

[33] W. Que, “Excitons in quantum dots with parabolic confinement,” *Phys.Rev.B*, Vol. 45, no. 19, pp.11036-11041 (1992).

[34] G. Park, O.B. Shchekin, D. L. Huffaker, and D. G. Deppe, “ Lasing from InGaAs/GaAs quantum dots with extended wavelength and well-defined harmonic oscillator energy levels,” *Appl. Phys. Lett.*,Vol.73,no.23, pp.3351-3353 (1998).

[35] A. J. Williamson, L. W. Wang and Alex Zunger, “Theoretical interpretation of the experimental electronic structure of lens-shaped self-assembled InAs/GaAs quantum dots,” *Phys. Rev. B*, no.19, Vol. 62, pp.12963-12977 (2000).

[36] K. H. Schmidt, G. Medeiros-Ribeiro, M. Oestreich, and P. M. Petroff, “Carrier relaxation and electronic structure in InAs self-assembled quantum dots ,”*Phys. Rev. B*, Vol. 54, no. 16, pp 11346-11353 (1996).

[37] D.G.Deppe, D.L. Huffakar, G. Park, and O.B. Shchekin, “ Quantum Dots: A new generation of semiconductor lasers?,”LEOS Newsletter, pp. 3-6, June,2000.

[38] G. Park, O. B. Shchekin, and D. G. Deppe, “Temperature dependence of gain saturation in multilevel quantum dot,” *IEEE J. Quantum Electron.* 36, no.9 ,pp.1065-1071 (2000).

- [39] T. Amano, T Sugaya, and K. Komori, “ Highest density 1.3 μm InAs quantum dots covered with gradient composition InGaAs strain reduced layer grown with an As_2 source using molecular beam epitaxy,” *Jap. J. of Appl. Phys.*, Vol.44, no.14,pp.L432-L434 (2005).
- [40] D. L. Huffaker, G. Park, Z. Zou, O. B. Shchekin, and D. G. Deppe, “1.3 μm room-temperature GaAs-based quantum-dot laser,” *Appl. Phys. Lett.* Vol.73 no.18, pp.2564-2566 (1998).
- [41] M. Arzberger, U. Kasberger, G. Bohm, and G. Abstreiter, “Influence of a thin AlAs cap layer on optical properties of self-assembled InAs/GaAs quantum dots,” *Appl. Phys. Lett.* Vol.75, no.25, pp.3968-3970 (1999) .
- [42] H. Kressel and J. K. Butler, “ Semiconductor lasers and hetrojunction LEDs,” Academic Press (1977).
- [43] B.S. Ryvkin, and E.A. Avrutin, “ Effect of carrier loss through waveguide layer recombination on the internal quantum efficiency in large-optical-cavity laser diodes,” *J. of Appl. Phys.*, Vol. 97, pp.113106 (2005).
- [44] A. Bruce Buckman, Guided-Wave Photonics (Saunders College Publishing, 1992) Chapter 2.
- [45] D.L Huffaker, G.Park, Z. Zou,O.B. Shchekin, and D.G. Deppe, “Continuous-wave low-threshold performance of 1.3- μm InGaAs-GaAs quantum-dot lasers,” *IEEE J. of Selected Topics in Quantum Electron*, Vol.6, no. 3, pp. 452-461 (2000).

- [46] Z. Zou, O.B. Shchekin, G. Park, D.L. Huffaker, and D. G. Deppe, "Threshold temperature dependence of lateral-cavity quantum-dot lasers," *IEEE Photon. Technol. Lett.*, Vol. 10, no. 12, pp. 1673 -1675 (1998).
- [47] W. Sheng and J. -P. Leburton, "Interband transition distributions in the optical spectra of InAs/GaAs self-assembled quantum dots," *Appl. Phys. Lett.*, 80, no.15, pp.2755-2757 (2002).
- [48] Dennis G. Deppe, H. Huang, Oleg B. Shchekin, "Modulation characteristics of quantum-dot lasers: the influence of p-type doping and the electronic density of states on obtaining high speed," *IEEE J. Quantum Electron*, Vol.38, no.12 , pp.1587-1593 (2002) .
- [49] B.S. Ryvkin, and E.A. Avrutin, "Improvement of differential quantum efficiency and power output by waveguide asymmetry in separate-confinement –structure diode lasers,"*IEEE Proc-Optoelectron*. Vol. 151, no 4, pp. 232-236 (2004).
- [50] A. Al-Muhanna, L. J. Mawst, , D. Botez, D. Z. Garbuzov, R.U. Martinelli, and J. C. Connolly, " 14.3 W quasi-continuous wave front-facet power from broad-waveguide Al-free 970 nm diode lasers,"*Appl. Phys. Lett.*, Vol. 71, no. 9, pp. 1142-1144 (1997).
- [51] D. Garbuzov, L. Xu, S. R. Forest, R.Menna, R. Martinelli, and J. C. Connolly, " 1.5 μm wavelength, SCH-MQW InGaAs/InP broadened –waveguide laser diodes with low internal loss an high output power," *Electron. Lett.*, Vol. 32, no. 18, pp.1717-1718 (1996).
- [52] S. Leu, F. Hohnsclorf, W.Stolz, R. Becker, A.Salzmann, and A. Greiling, " C and O incorporation in (AlGa)As epitaxial layers grown by MOVPE using TBAs," *J. of crystal Growth*, Vol. 195, pp. 98-104 (1995).

- [53] W.B. Joyce, and R.W. Dixon “Thermal resistance of heterostructure lasers”, *J. of Appl. Phys.*, vol. 46, no.2, p. 855-862, (1975).
- [54] V. L. Rideout,” A review of theory and technology for Ohmic contacts to group III-V compound semiconductors,” *Solid State Electron.*, Vol. 18, no. 6, pp. 541 (1975).
- [55] S. Slivken, “ Quantum Cascade lasers Grown by Gas-source Molecular beam Epitaxy,” Ph.D Dissertation, Evanston, Illinois, June (2002).
- [56] R.E Kazarinov, and R.A. Suris, “ Possibility of the Amplification of Electromagnetic Waves in a Semiconductor With a Spuerlattice,” *Soviet Phys. Semiconductors*, 5, pp. 707-709 (1971).
- [57] J. Faist, F. Capasso, C. Sirtori, D.L. Sivco, and A.Y. Cho, ‘Quantum Cascade Lasers,” *Semiconductors and Semimetals*, Vol. 66, Chapter 1(Academic Press, 2000).
- [58] H. Page, P. Kruck, S. Barbieri, C. Sirtori, M. Stellmacher, and J. Nagle, “ High peak power (1.1 W) Al(GaAs) quantum cascade laser emitting at 9.7 μm ,” *Electron, Lett.* Vol. 35, no. 21, pp. 1848-1849 (1999).
- [59] J. S. Yu, S. Slivken, A. Evans, S.R. Darvish, J. Nguyen and M. Razeghi, “ High-power $\lambda\sim 9.5 \mu\text{m}$ quantum-cascade lasers operating above room temperature in continuous-wave mode,” *Appl. Phys. Lett.*, Vol. 88, pp.091113 (2006).
- [60] C. Sirtori, “GaAs Quantum Cascade Lasers: Fundamental and Performance,” © EDP Sciences (2002).
- [61] J. Faist, F. Capasso, C. Sirtori C., D. L. Sivco, J.N. Baillaregeon ,A. L. Hutchinson ,A. Y. Cho and S. N. G. Chu., *Appl. Phys. Lett.*, Vol. 68, pp. 3680-3682 (1996).

[62] A. Tredicucci ,F. Capasso , C. Sirtori , D. L. Sivco ,A. L. Hutchinson , and A. Y. Cho,“ A Multiwavelength semiconductor laser,” *Nature*, Vol. 396, pp. 350-352 (1998).

[63] <http://www.bell-labs.com/org/physicalsciences/psr/qcl>

[64] S. Slivken, V. I. Litvinov, and M. Razeghi, “ Relaxation kinetics in quantum cascade lasers,” *J. of Appl. Phys.*,Vol. 85, no.2 , pp.665-671 (1999).

[65] S. -C. Lee, I. Galbraith, and C. R. Pidgeon, “ Influence of electron temperature and carrier concentration on electron-LO phonon intersubband scattering in wide GaAs/Al_xGa_{1-x}As quantum wells,” *Phys. Rev. B.*, Vol. 52, no. 3, pp. 1874-1881 (1995).

[66] Paul Harrison, “ *Quantum Wells, Wires and Dots: Theoretical and Computational Physics*”, John Willey & Sons, Ltd.

[67] J. Faist, F. Capasso, C. Sirtori, D.L. Sivco, A.L. Hutchinson, M.S. Hybersten, and A.Y. Cho,” Quantum Cascade Lasers without intersubband population inversion,” *Phys.Rev.Lett.*,Vol.76,no.3, pp.411-414 (1996).

[68] J. S .Yu, A. Evans, J. David, L. Doris, S. Slivken, and M. Razeghi, “Cavity-length effects of high temperature high-power continuous-wave characteristics in quantum-cascade lasers,” *Appl. Phys. Lett.*,Vol.83,no.25,pp.5136-5138 (2003).

[69] J. S. Yu, S. Slivken, A. Evans, L. Doris, and M. Razeghi, “ High-power continuous-wave operation of a 6 μm quantum-cascade laser at room temperature,” *Appl. Phys. Lett.*, Vol. 83, no. 13, pp.2503-2505 (2003).

- [70] A.Evans, J. S. Yu, S. Slivken, and M. Razeghi, “Continuous-wave operation of $\lambda\sim 4.8\ \mu\text{m}$ quantum-cascade lasers at room temperature,” *Applied Phys. Lett.*, Vol. 85, no.12,pp. 2166-2168 (2004).
- [71] A. Evans,J. Nguyen, S.Slivken, J.S. Yu, S.R.Darvish, and M. Razeghi, “ Quantum-cascade lasers operating in continuous –wave mode above $90^0\ \text{C}$ at $\lambda\sim 5.25\ \mu\text{m}$,” *Appl. Phys. Lett.*,Vol.. 88, pp.051105 (2006).
- [72] J. Pipreck, “Cavity length effects on internal loss and quantum efficiency of multi-quantum-well lasers,” *IEEE J. of Selected Topics in Quantum Electron.*, Vol. 5 , no. 3, pp. 643-647 (1999).
- [73] J. S .Yu, A. Evans, J. David, L. Doris, S. Slivken, and M. Razeghi, “Cavity-length effects of high temperature high-power continuous-wave characteristics in quantum-cascade lasers,” *Appl. Phys. Lett.*,Vol.83,no.25,pp.5136-5138 (2003).
- [74] A.Dmitriev, and R. A . Suris, “Quantum Cascade Lasers based on quantum dot superlattice,” *Phys. Stat. Sol.(a)*, Vol.202, no. 6, pp.987-991 (2005).
- [75] F. Klopf, J. P. Reithmaier, A. Forchel, P. Collot, M. Krakowski, and M. Calligaro, “ High-performance 980 nm quantum dot lasers for high power applications,”*Electron.Lett.*,Vol. 37, no. 6 pp. 353-354 (2001).

VITA

Sonia Quadery was born in Chittagong, Bangladesh on May 19, 1975, the daughter of Suraiya Quadery and Lutful Anwar Quadery. After completing her Secondary School Certificate Examination from Bangladesh Mohila Somity Girls High School, Chittagong, she entered Chittagong College, Chittagong. From this college, she secured 13th position in the combined merit list in the Higher Secondary Certificate Examination under Comilla Board. Then she enrolled at the Applied Physics & Electronics Department of Dhaka University, Bangladesh in 1994. She completed her Bachelor of Science with Honours in Applied Physics & Electronics in 1998 securing 1st class 2nd position and Master of Science in Applied Physics & Electronics in 2000 securing 1st class 1st position. In May, 2001 she entered The University of Texas at Austin. She obtained the Masters of Science degree in Electrical Engineering from the University of Texas at Austin in August 2003.

Permanent Address:

“Sonar Tory”

61, Panchlaish Residential Area,

Chittagong-4000

Bangladesh

This dissertation was typed by the author.